Multiflavor bosonic Hubbard models in the first excited Bloch band of an optical lattice

A. Isacsson[1,2] and S. M. Girvin[2]
[1]*NORDITA, Blegdamsvej 17, Copenhagen Oe, DK-2100, Denmark*
[2]*Department of Physics, Yale University, P. O. Box 208120, New Haven, Connecticut 06520-8120, USA*
(Received 27 June 2005; published 3 November 2005)

We propose that by exciting ultracold atoms from the zeroth to the first Bloch band in an optical lattice, multiflavor bosonic Hubbard Hamiltonians can be realized in a different way. In these systems, each flavor hops in a separate direction and on-site exchange terms allow pairwise conversion between different flavors. Using band-structure calculations, we determine the parameters entering these Hamiltonians and derive the mean-field ground-state phase diagram for two effective Hamiltonians (two dimensional, two flavors, and three dimensional, three flavors). Further, we estimate the stability of atoms in the first band using second-order perturbation theory and find lifetimes that can be considerably (10–100 times) longer than the relevant time scale associated with intersite hopping dynamics, suggesting that quasiequilibrium can be achieved in these metastable states.

DOI: 10.1103/PhysRevA.72.053604 PACS number(s): 03.75.Lm, 03.75.Mn, 73.43.Nq

I. INTRODUCTION

The possibility to trap and manipulate the atoms in a Bose-Einstein condensate using standing-wave laser beams [1–6] has led to a renewal of interest in basic solid state models. In such systems, the atoms experience a periodic potential from an optical lattice leading to formation of band structure in the energy spectrum. These bands have been investigated in experiments [7].

In the spectroscopy experiments in Ref. [7], the atoms experienced a periodic potential in only one direction, being free to move on a much larger length scale in the other directions. This implied that interactions between atoms could be ignored. If the atoms are confined to reside on the sites of a lattice in three dimensions, interactions become important. As a result, it was shown theoretically [3], and subsequently also experimentally [5], that a system of interacting cold atoms, residing in the lowest Bloch band of the periodic potential, maps onto a bosonic Hubbard model. This model is of great theoretical interest since it exhibits a quantum phase transition [8–11] between ground states where the atoms are localized (Mott insulator) and where they are delocalized (superfluid) as the strength of the hopping relative to the interatomic interaction is varied. The dynamics of particles under the influence of changes in the Hamiltonian (such as lattice tilts or rapid changes in the particle interaction strength) has also proved interesting [4–6,12,13].

Another development is an interest in the idea of mixing bosonic atoms of different flavors in the lattice [14–19]. Several ways of achieving multiple flavors have been suggested, including using atoms of different species and exploiting different internal atomic states.

So far, experiments on strongly interacting atoms in three-dimensional optical lattices have been restricted to atoms in the lowest (zeroth) Bloch band. Recently Scarola and Das Sarma considered the possibility of supersolid phases within the first excited Bloch band of an optical lattice [20].

In this paper, the theory of atoms in the two lowest (zeroth and first) Bloch bands of a three-dimensional optical lattice is considered. We show here that, due to the lack of available phase space for the decay products, such excited states can (in some parameter ranges) have lifetimes much longer than the characteristic time scales for intersite hopping. Thus it should be possible to establish quasiequilibrium within the manifold of these metastable states.

We find that it is possible in this way to realize effective multispecies bosonic Hubbard Hamiltonians. Depending on the choice of lattice depths the number of degenerate bands varies and we find effective models involving n flavors of bosons, where n can be 1, 2, or 3. These flavors correspond to the three different possible nodal planes in the excited-state wave function such as the one illustrated in Fig. 1. We will show that a characteristic of these Hamiltonians is that (to a good approximation) each flavor can hop in only one direction [i.e., X (nodal plane) particles can hop in only the x direction, etc.]. Neglecting interactions we would then have n interpenetrating one-dimensional free Bose gases, one for each column (or row) in the lattice. Allowing intraspecies interactions converts these one-dimensional gases into Luttinger liquids (or, if the interactions are strong enough, and the mean particle number per site is an integer, into Mott insulators). We show below that, besides intraspecies interactions, the full interaction also includes on-site interspecies conversion terms that allow atoms to change flavor in pairs. Thus for example, two X particles constrained to move along a single x column can collide, turn into Y particles, and move away along a y column. Such processes lead to interesting quantum dynamics for this coupled set of interpenetrating Luttinger liquids.

As will be seen, the anisotropic nature of the hopping in conjunction with the pairwise conversion leads to Hamiltonians with an infinite but subextensive set of Z_2-gauge symmetries intermediate between local and global. Such infinite symmetries have been found in certain frustrated spin models [21–24] and in a "Bose metal" model [25] and are known to cause dimensional reduction in some cases [21,22,24]. We will see below how this dimensional reduction appears in a simple way in this system.

A related *global* Z_2 symmetry and associated Ising order parameter appear in problems involving boson pairing due to

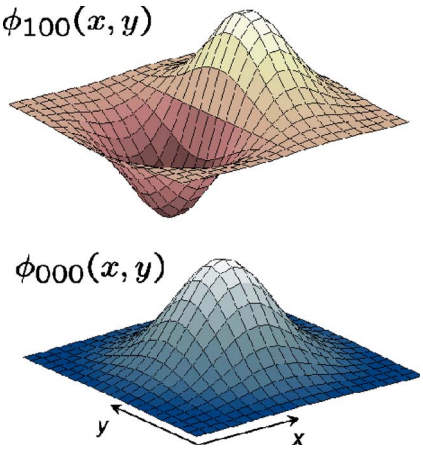

FIG. 1. (Color online) On-site Wannier wave functions in the harmonic oscillator approximation. The localized wave functions are to a good approximation described by harmonic oscillator wave functions localized in each well. Above is drawn the wave functions $\phi_{(0,0,0)}(\mathbf{r})$ (plotted in the plane $z=0$) formed by the zeroth-band Bloch functions and the wave function $\phi_{(1,0,0)}(\mathbf{r})$ formed by the zeroth-band Bloch functions in the y and z directions and the Bloch functions from the first band in the x direction. These are approximately harmonic oscillator states, $\phi_{(0,0,0)}(\mathbf{r}) \sim \exp[-\alpha(x^2+y^2+z^2)]$ and $\phi_{(1,0,0)}(\mathbf{r}) \sim x \exp[-\alpha(x^2+y^2+z^2)]$, where the parameter α is determined by the curvature of the optical lattice potential near its minimum. Similarly $\phi_{(0,1,0)}(\mathbf{r}) \sim y\phi_{(0,0,0)}(\mathbf{r})$ and $\phi_{(0,0,1)}(\mathbf{r}) \sim z\phi_{(0,0,0)}(\mathbf{r})$.

attractive interactions mediated by Feshbach resonances. In that case the symmetry appears due to a conversion term that connects pairs of bosons with a distinct molecular field. This can lead to exotic states in which pairs of bosons are condensed but single bosons are not and in which half vortices are permitted [26,27].

Further, due to strong interatomic repulsion, the ground state in three dimensions (3D) (three flavors) breaks a kind of chiral symmetry and displays an additional accidental ground-state degeneracy at the mean-field level. A similar situation occurs for special parameter values in frustrated XY models, where parallel zero-energy domain walls can be inserted [28]. The outline of this paper is as follows. In Sec. II the appropriate generalization of the bosonic Hubbard model is introduced along with numerical values of the parameters entering the Hamiltonians obtained from band-structure calculations for various lattice depths. Then, in Sec. III, the aforementioned effective Hamiltonians for atoms in the first band are derived for three particular choices of relative lattice depths in the xyz directions. Using simple mean-field theory we sketch the ground-state phase diagrams in Sec. IV and in Sec. V we discuss how the superfluid phases are reflected in the interference pattern in an experimental situation. Finally, in Sec. VI, treating the interaction perturbatively to second order, we estimate the lifetime of a population-inverted state (all atoms residing entirely in the first excited band).

II. GENERAL LATTICE HAMILTONIAN

The starting point is the Hamiltonian for weakly interacting bosons of mass m in an external potential [29],

$$\hat{H} = \int d^3\mathbf{x}\, \hat{\psi}^\dagger(\mathbf{x})\left(-\frac{\hbar^2}{2m}\nabla^2 + V_O(\mathbf{x}) + V_T(\mathbf{x})\right)\hat{\psi}(\mathbf{x}) + \frac{1}{2}\frac{4\pi a_s\hbar^2}{m}\int d^3\mathbf{x}\, \hat{\psi}^\dagger(\mathbf{x})\hat{\psi}^\dagger(\mathbf{x})\hat{\psi}(\mathbf{x})\hat{\psi}(\mathbf{x}), \quad (1)$$

where a_s is the s-wave scattering length. The external potential has two contributions V_O and V_T corresponding to the lattice potential and the magnetic trapping potential. Denoting the wavelength of the lasers by $\lambda \equiv 2a$, a being the lattice spacing, the former can be written

$$V_O(\mathbf{x}) = \sum_{i=x,y,z} V_{0i}\sin^2\left(\frac{2\pi}{\lambda}x_i\right), \quad \{x_i\}_{i=x,y,z} = (x,y,z).$$

The positional dependence of the magnetic trapping potential $V_T = \frac{1}{2}m\Sigma_{i=x,y,z}\Omega_i^2 x_i^2$ is much weaker than that of the lattice, i.e., $\Omega_i \ll (2\pi/\lambda)\sqrt{(2V_{0i}/m)}$ and will be ignored in the remainder of this paper. One should be aware though that this term has been shown to influence, for instance, the phase diagram of the single-flavor bosonic Hubbard model [30–37].

For the cubic lattices considered here, the Wannier functions corresponding to the noninteracting part of the Hamiltonian in Eq. (1) can be written

$$\phi_{\mathbf{n}}(\mathbf{x}-\mathbf{R}_{\mathbf{m}}) = \prod_{i=x,y,z}\phi_{n_i}^{(i)}(x_i - m_i a).$$

Here the boldface vectors $\mathbf{n}$ and $\mathbf{m}$ are integer triplets (n_x,n_y,n_z) and (m_x,m_y,m_z) which represent band indices and lattice sites, respectively, i.e.,

$$\mathbf{R}_{\mathbf{m}} = m_x a\hat{x} + m_y a\hat{y} + m_z a\hat{z}.$$

These functions are to a good approximation described by localized harmonic oscillator wave functions sketched in Fig. 1. The completeness of the Wannier functions allows the field operators to be expanded as

$$\hat{\psi}(\mathbf{x}) = \sum_{\mathbf{m}}\sum_{\mathbf{n}}\hat{d}_{\mathbf{n}}(\mathbf{m})\phi_{\mathbf{n}}(\mathbf{x}-\mathbf{R}_{\mathbf{m}}).$$

The operators $\hat{d}_{\mathbf{n}}^\dagger(\mathbf{m})$ and $\hat{d}_{\mathbf{n}}(\mathbf{m})$, which are the creation and annihilation operators of bosons at site $\mathbf{m}$ and with band index $\mathbf{n}$, obey the Bose commutation relations $[\hat{d}_{\mathbf{n}}(\mathbf{m}),\hat{d}_{\mathbf{n}'}^\dagger(\mathbf{m}')] = \delta_{\mathbf{n},\mathbf{n}'}\delta_{\mathbf{m},\mathbf{m}'}$. Ignoring all hopping other than nearest-neighbor hopping and all interactions other than on-site interactions, the Hamiltonian in Eq. (1) can be written

$$\hat{H} \approx \sum_{\mathbf{m}}\sum_{\mathbf{n}} E_{\mathbf{n}}(\mathbf{m})\hat{d}_{\mathbf{n}}^\dagger(\mathbf{m})\hat{d}_{\mathbf{n}}(\mathbf{m}) - \sum_{i=x,y,z}\sum_{\mathbf{n}} t_{\mathbf{n}}^{(i)}\sum_{\langle\mathbf{m},\mathbf{m}'\rangle_i}[\hat{d}_{\mathbf{n}}^\dagger(\mathbf{m})\hat{d}_{\mathbf{n}}(\mathbf{m}') + \hat{d}_{\mathbf{n}}^\dagger(\mathbf{m}')\hat{d}_{\mathbf{n}}(\mathbf{m})] + \frac{1}{2}\sum_{\mathbf{n}_1,\mathbf{n}_2,\mathbf{n}_3,\mathbf{n}_4}\sum_{\mathbf{m}} U(\mathbf{n}_1,\mathbf{n}_2,\mathbf{n}_3,\mathbf{n}_4) \times[\hat{d}_{\mathbf{n}_1}^\dagger(\mathbf{m})\hat{d}_{\mathbf{n}_2}^\dagger(\mathbf{m})\hat{d}_{\mathbf{n}_3}(\mathbf{m})\hat{d}_{\mathbf{n}_4}(\mathbf{m})]. \quad (2)$$

Here, the on-site interaction energies are defined as

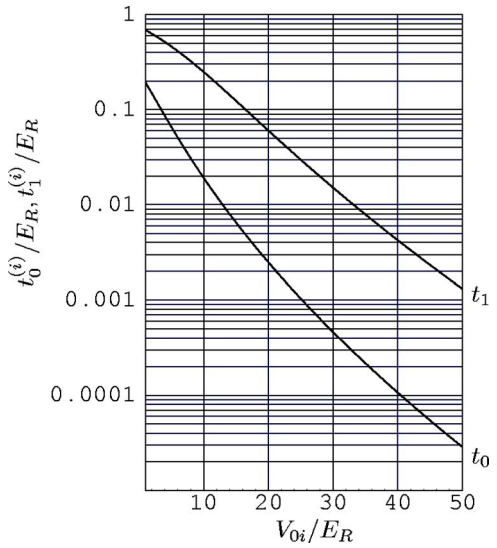

FIG. 2. (Color online) Hopping energies $t_1^{(i)}$ and $t_0^{(i)}$ in units of the recoil energy as functions of lattice depth V_{0i} in the hopping direction. The upper line is the hopping energy $t_1^{(i)}$ for atoms in the first Bloch band hopping between nearest-neighbor wells while the lower line $t_0^{(i)}$ corresponds to atoms in the zeroth band.

$$U(\mathbf{n}_1,\mathbf{n}_2,\mathbf{n}_3,\mathbf{n}_4) \equiv \frac{4\pi a_s \hbar^2}{m} \int d^3\mathbf{x}\, \phi^*_{\mathbf{n}_1}(\mathbf{x})\phi^*_{\mathbf{n}_2}(\mathbf{x})\phi_{\mathbf{n}_3}(\mathbf{x})\phi_{\mathbf{n}_4}(\mathbf{x}), \tag{3}$$

while the energies $E_{\mathbf{n}}(\mathbf{m})$ and the hopping energies $t_{\mathbf{n}}^{(i)}$ are given by

$$E_{\mathbf{n}}(\mathbf{m}) \equiv \int d^3\mathbf{x}\, \phi^*_{\mathbf{n}}(\mathbf{x})\left(-\frac{\hbar^2}{2m}\nabla^2 + V_O(\mathbf{x})\right)\phi_{\mathbf{n}}(\mathbf{x}), \tag{4}$$

$$t_{\mathbf{n}}^{(i)} \equiv \int dx_i\, \phi^{(i)*}_{n_i}(x_i)\left(-\frac{\hbar^2}{2m}\frac{\partial^2}{\partial x_i^2} + V_{0i}(x_i)\right)\phi^{(i)}_{n_i}(x_i + a). \tag{5}$$

Note that the energies $t_{\mathbf{n}}^{(i)}$ for hopping in the x_i direction depend only on the lattice depth V_{0i} in the corresponding direction and the ith component n_i of the band index $\mathbf{n}$. The notation $\langle \mathbf{m},\mathbf{m}'\rangle_i$ in Eq. (2) indicates that the sum should be carried out over nearest-neighbor sites $\mathbf{m}$ and $\mathbf{m}'$ in the x_i direction. One could for instance write

$$\sum_{\langle \mathbf{m},\mathbf{m}'\rangle_y} \equiv \sum_{\mathbf{m}} \sum_{\mathbf{m}'} \delta_{m_x,m'_x}\delta_{m_z,m'_z}\delta_{m_y,m'_y+1}.$$

It is straightforward to numerically solve the noninteracting Schrödinger equation and find the energies in expressions (3)–(5) above. In doing so, it is convenient to first switch to dimensionless units. Thus, we measure length in units of the inverse wave vector and potential depth in units of the recoil energy E_R, i.e., $\xi_i \equiv (2\pi/\lambda)x_i$ and $v_{0i} \equiv V_{0i}/E_R$, with $E_R \equiv (\hbar^2/2m)(2\pi/\lambda)^2$.

The hopping energies for the two lowest bands, obtained from band-structure calculations, are shown in Fig. 2 as functions of lattice depth. To get the on-site interaction [Eq. (3)] in a suitable form to use later on in the paper we define dimensionless overlap integrals

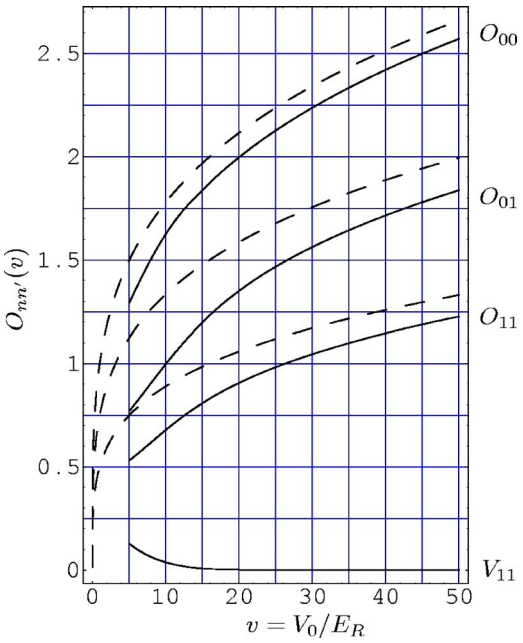

FIG. 3. (Color online) Overlap integrals $O_{nn'}(v)$ defined in Eq. (6). Solid lines, from top to bottom, O_{00},O_{01},O_{11}, obtained from numerical calculations. The dashed lines correspond to the values in Eq. (7) obtained by using harmonic oscillator wave functions determined from the curvature of the potential at the well bottom. For comparison V_{11}, the largest of the nearest-neighbor overlap integrals, is also shown.

$$O_{nn'}(v) \equiv \sqrt{2\pi}\int d\xi |\tilde{\phi}_n(v;\xi)|^2 |\tilde{\phi}_{n'}(v;\xi)|^2, \tag{6}$$

where dimensionless Wannier wave functions

$$\tilde{\phi}_n(v,\xi) \equiv \sqrt{\frac{\lambda}{2\pi}}\phi_n(vE_R;\xi\lambda/2\pi)$$

have been introduced. The dependence on v in these functions is parametric, i.e., $\phi_n(vE_R;\xi\lambda/2\pi)$ is the Wannier function corresponding to the one-dimensional noninteracting problem with potential depth vE_R. The variable n denotes the band index.

Approximating the Wannier functions with harmonic oscillator wave functions corresponding to the curvature at the bottom of each well, one finds approximate values for the overlap integrals,

$$O^{\mathrm{ho}}_{nn'}(v) = \frac{3^{nn'}}{2^{n+n'}}v^{1/4}. \tag{7}$$

A comparison between these values for the overlap integrals and those obtained from band-structure calculations is shown in Fig. 3.

In writing the Hamiltonian in Eq. (2) we have omitted interaction terms resulting from nearest-neighbor interactions, both for atoms in the same band and for atoms in

different bands. Such terms can have a dramatic impact on the physics as shown in Ref. [20]. In what follows we will, however, only consider atoms in the zeroth and first bands. In this case, for lattice strengths $V_0 > 30E_R$ which are physically relevant here, we have found (numerically calculating the nearest-neighbor overlaps, using the Wannier functions obtained from band-structure calculations) that the largest of these terms, the nearest-neighbor interaction of two atoms in the same excited band, are (for $V_0 > 30E_R$) always at least a factor 10^{-2} smaller than the hopping energies t and can thus safely be neglected. The corresponding dimensionless overlap integral

$$V_{11}(v) \equiv 2\sqrt{2\pi} \int d\xi |\tilde{\phi}_1(v;\xi)|^2 |\tilde{\phi}_1(v;\xi+\pi)|^2 \qquad (8)$$

is shown for comparison in Fig. 3. For more highly occupied bands and lower lattice heights the Wannier functions will be more delocalized and such terms cannot be neglected leading to interesting effects including, for instance, conditional hopping terms [20].

III. EFFECTIVE HAMILTONIANS FOR ATOMS IN THE FIRST EXCITED BAND

In this section we will focus on the metastable situation having all atoms in the first Bloch band(s) of the lattice. It is quite easy to achieve such a situation, i.e., consider an initial moment of time when the optical lattice has been loaded with atoms in the lowest Bloch band, $\mathbf{n}=(0,0,0)$. The anharmonicity of the lattice well potential allows one to treat the vibrational degree of freedom as a two-level system. If one singles out, say, the x direction, then, by applying an appropriate vibrational π pulse, i.e., "shaking" the lattice in this direction with a frequency on resonance with the transition $\hbar\omega = E_{(1,0,0)} - E_{(0,0,0)}$, the state can be inverted and the atoms excited to states with band index $\mathbf{n}=(1,0,0)$. It is well known from NMR physics that for such a π pulse to be able to efficiently invert the entire population it has to be strong, i.e., the duration needs to be short compared to both hopping and interaction time scales, such that the pulse "covers" the entire inhomogeneously broadened line shape.

The simplest starting state would be the Mott insulator state with one boson per site in the lowest band. In a typical experimental setup, the parabolic confining potential will cause the population of each well to vary and the system will be in a state with regions of Mott insulators with different filling factors. It is, however, easy to confirm (by direct simulation) that even in this case, taking interactions into account, a pulse shape can be tailored that will invert the population simultaneously for regions with different filling factors provided a deep enough lattice is used.

Another way of preparing the initial state is to use the method recently demonstrated by Browaeys *et al.* [38]. By loading a condensate into a moving 1D lattice and applying a subsequent acceleration the condensate can be prepared in the lowest-energy state (quasimomentum $k=\pi/a$) in the first Bloch band. The situation desired in this paper can then be obtained by ramping up the lattice in the two remaining (perpendicular) directions adiabatically. The natural question regarding the lifetime of the resulting metastable state will be considered in Sec. VI.

The subsequent dynamics of atoms in the first band(s) is then predominantly governed by some subset of the terms in Eq. (2). This relevant subset will be referred to as the effective Hamiltonian. We will treat three different regimes of values for the lattice potentials V_{0i} which lead to effective Hamiltonians with one, two, and three flavors, respectively. The three scenarios are (1) $V_{0x} \ll V_{0y}, V_{0z}$ (1D, single flavor); (2) $V_{0x} = V_{0y} \ll V_{0z}$ (2D, two flavors); (3) $V_{0x} = V_{0y} = V_{0z}$ (3D, three flavors). As indicated, the numbers of particle flavors as well as the dimensionalities in the effective Hamiltonians vary.

The reason for the different numbers of flavors becomes clear if one considers the restrictions on the final states into which two atoms may scatter due to the interatomic interaction; the presence or absence of such states can be inferred from the presence or absence of degenerate, or nearly degenerate, levels in the energy spectrum of the noninteracting system. Take, for example, the second scenario above with $V_{0x} = V_{0y} \ll V_{0z}$ and all atoms initially in a state with index $\mathbf{n}=(1,0,0)$; then, due to the on-site interatomic interaction these atoms can scatter elastically into a state with index $\mathbf{n}=(0,1,0)$ through a first-order process connecting different degenerate states. Further, it is easy to show that scattering resulting in states with other indices, for instance $\mathbf{n}=(0,0,1)$, is possible only through higher-order processes if energy (and also parity) is to be conserved, and can safely be ignored if the gas is dilute. Hence, the atoms can, at a formal level, be divided into two flavors: an X flavor corresponding to atoms in $\mathbf{n}=(1,0,0)$ and a Y flavor in $\mathbf{n}=(0,1,0)$. By the same argument one can see how the one- and three-flavor situations arise.

Apart from having different number of flavors the dimensionalities of the effective Hamiltonians differ. To understand this consider again the second case above, $V_{0x} = V_{0y} \ll V_{0z}$, with particles in the excited bands $\mathbf{n}=(1,0,0)$ and $\mathbf{n}=(0,1,0)$ corresponding to X and Y flavors. For the X flavor, hopping in the x direction has a matrix element $t_1^{(x)}(V_{0x})$ while hopping in the y and z directions have matrix elements $t_0^{(y)}(V_{0x})$ and $t_0^{(z)}(V_{0z})$, respectively. Looking at Fig. 2 it is then clear that, to a good approximation, the X particles can hop only in the x direction while hopping in the y and z directions is strongly (exponentially) suppressed. Similarly, the Y particles can hop only in the y direction and all hopping occurs only in the x-y plane; hence the 2D character. A similar argument holds for the three-flavor case where in addition to the X and Y particles, there are Z particles hopping in the z direction.

The effective Hamiltonians also contain terms arising from the on-site interaction. Apart from the terms that repel atoms from each other, the symmetry of the on-site interaction allows, say, two X particles moving in the x direction to collide and convert into two Y particles which thereafter move off in the y direction. The time-reversed process can, of course, also occur. Thus, the number of particles of each flavor is not conserved and there is a pairwise exchange of particles of different flavors.

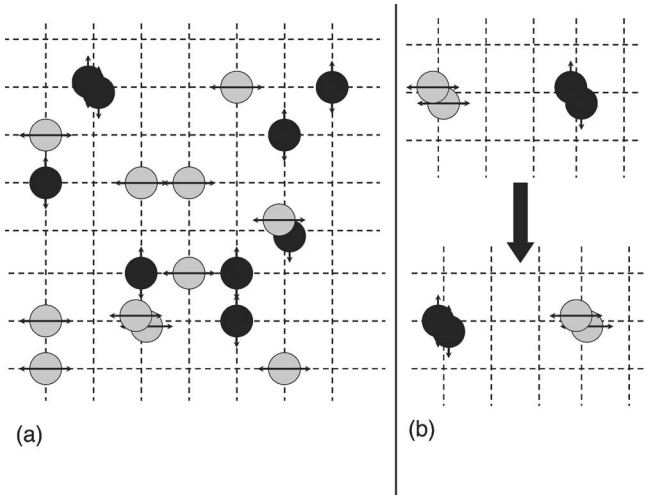

FIG. 4. (a) The Hamiltonian in Eq. (12) describes a 2D system where atoms, which can formally be thought of as having two different flavors (same type of atoms but in different localized on-site orbitals), hop around subject to on-site repulsive interactions. One flavor, the X flavor, can hop only in the x direction whereas the other, Y flavor, can hop only in the y direction. (b) Conversion process. The conversion term in Eq. (12) takes two X atoms on the same lattice site and turns them into two Y atoms, or vice versa.

The anisotropy of hopping and the flavor conversion process is schematically depicted for the 2D (two-flavor) case in Fig. 4. Particles of X flavor are shown in gray while the Y flavor is drawn in black.

Below, we give the effective Hamiltonians for all three different cases listed above.

A. 1D Hamiltonian, single flavor ($V_{0x} \ll V_{0y} = V_{0z}$)

The first case to be considered is when $V_{0x} \ll V_{0y} = V_{0z}$ and only states with band index $\mathbf{n}=(1,0,0)$ [and possibly some residual atoms in $\mathbf{n}=(0,0,0)$] are occupied. In anticipation of the other effective Hamiltonians it is convenient to introduce for the X flavor the creation and destruction operators $\hat{X}^\dagger$ and $\hat{X}$, i.e.,

$$\hat{X}_{\mathbf{m}} \equiv \hat{d}_{(1,0,0)}(\mathbf{m}), \quad \hat{X}^\dagger_{\mathbf{m}} \equiv \hat{d}^\dagger_{(1,0,0)}(\mathbf{m}),$$

$$\hat{n}^{(x)}_{\mathbf{m}} \equiv \hat{X}^\dagger_{\mathbf{m}}\hat{X}_{\mathbf{m}}, \quad \hat{n}^{(0)}_{\mathbf{m}} \equiv \hat{d}^\dagger_{(0,0,0)}(\mathbf{m})\hat{d}_{(0,0,0)}(\mathbf{m}). \tag{9}$$

The effective Hamiltonian is then essentially that of a quasi-one-dimensional bosonic Hubbard model,

$$H_{1D} = \sum_{\mathbf{m}} \hat{n}^{(x)}_{\mathbf{m}} \left(E_x(\mathbf{m}) + U_{0x}\hat{n}^{(0)}_{\mathbf{m}} + \frac{U_{xx}}{2}(\hat{n}^{(x)}_{\mathbf{m}} - 1) \right) - t \sum_{\langle \mathbf{m},\mathbf{m}' \rangle_x} (\hat{X}^\dagger_{\mathbf{m}}\hat{X}_{\mathbf{m}'} + \text{H.c.}).$$

The energies $t \equiv t_1^{(x)}$, U_{0x}, and U_{xx} arise from the interwell tunneling and the interatomic interaction, respectively. The presence of atoms residing in the lowest band leads to an additional effective on-site energy and can be absorbed in the on-site energies $E_x(\mathbf{m})$ $(s=x,y,z)$. Although this single-flavor model is equivalent to a single-flavor model in the zeroth Bloch band, the additional random on-site potential resulting from residual atoms could be exploited in the study of the disordered Bose-Hubbard system.

The parameters entering the Hamiltonian (10) are conveniently expressed as

$$U_{xx} = 2\sqrt{2\pi}E_R\left(\frac{a_s}{a}\right)O_{00}(v_{0y})O_{00}(v_{0z})O_{11}(v_{0x}), \tag{10}$$

$$U_{0x} = 2U_{xx}O_{01}(v_{0x})/O_{11}(v_{0x}). \tag{11}$$

B. 2D Hamiltonian, two flavors ($V_{0x} = V_{0y} \ll V_{0z}$)

To simplify the notation for the case $V_{0x} = V_{0y} \ll V_{0z}$, we introduce new letters for the creation and annihilation operators $\hat{Y}_{\mathbf{m}} \equiv \hat{d}_{(0,1,0)}(\mathbf{m})$, $\hat{n}^{(y)}_{\mathbf{m}} \equiv \hat{Y}^\dagger_{\mathbf{m}}\hat{Y}_{\mathbf{m}}$. Then the Hamiltonian governing atoms in the excited bands becomes

$$H_{2D} = \sum_{s=x,y}\sum_{\mathbf{m}} E_s(\mathbf{m})\hat{n}^{(s)}_{\mathbf{m}} + \sum_{s=x,y}\frac{U_{ss}}{2}\sum_{\mathbf{m}} \hat{n}^{(s)}_{\mathbf{m}}(\hat{n}^{(s)}_{\mathbf{m}} - 1) - t\sum_{\langle \mathbf{m},\mathbf{m}' \rangle_y} (\hat{Y}^\dagger_{\mathbf{m}}\hat{Y}_{\mathbf{m}'} + \text{H.c.}) - t\sum_{\langle \mathbf{m},\mathbf{m}' \rangle_x} (\hat{X}^\dagger_{\mathbf{m}}\hat{X}_{\mathbf{m}'} + \text{H.c.}\,.) + U_{xy}\sum_{\mathbf{m}} \hat{n}^{(x)}_{\mathbf{m}}\hat{n}^{(y)}_{\mathbf{m}} + \frac{U_{xy}}{2}\sum_{\mathbf{m}} (\hat{X}^\dagger_{\mathbf{m}}\hat{X}^\dagger_{\mathbf{m}}\hat{Y}_{\mathbf{m}}\hat{Y}_{\mathbf{m}} + \text{H.c.}) \tag{12}$$

Again, the energy U_{xy} arises from the interatomic interaction and depends on the lattice depth. Note that this two-flavor bosonic Hubbard Hamiltonian differs in an important aspect from previously studied two-flavor systems: the presence of the last term that mixes the two flavors. Hence, the interatomic interaction leads to a "Josephson term" that allows for the conversion of two X atoms into two Y atoms, and vice versa. The coefficients $U_{yy} = U_{xx}$ are given by the same expression as in the 1D case while

$$U_{xy} = 2\sqrt{2\pi}E_R\left(\frac{a_s}{a}\right)O_{00}(v_{0z})O_{01}(v_{0x})^2. \tag{13}$$

Figure 4 illustrates the dynamics in the 2D (two-flavor) situation.

C. 3D Hamiltonian, three flavors ($V_{0x} = V_{0y} = V_{0z}$)

The generalization of the above Hamiltonian to the case when $V_{0x} = V_{0y} = V_{0z}$ is straightforward. Introducing a third flavor $\hat{Z}_{\mathbf{m}} \equiv \hat{d}_{(0,0,1)}(\mathbf{m})$, $\hat{n}^{(z)}_{\mathbf{m}} \equiv \hat{Z}^\dagger_{\mathbf{m}}\hat{Z}_{\mathbf{m}}$, one may write an effective Hamiltonian as

$$H_{3D} = \sum_{s=x,y,z} \sum_{\mathbf{m}} \left(E_s(\mathbf{m}) \hat{n}_{\mathbf{m}}^{(s)} + \frac{U_{ss}}{2} \hat{n}_{\mathbf{m}}^{(s)} (\hat{n}_{\mathbf{m}}^{(s)} - 1) \right) + \sum_{s \neq s'} \sum_{\mathbf{m}} U_{ss'} \left(\hat{n}_{\mathbf{m}}^{(s)} \hat{n}_{\mathbf{m}}^{(s')} + \frac{1}{2} (\hat{s}_{\mathbf{m}}^{\dagger} \hat{s}_{\mathbf{m}}^{\dagger} \hat{s}'_{\mathbf{m}} \hat{s}'_{\mathbf{m}} + \text{H.c.}) \right) - t \sum_{s=X,Y,Z} \sum_{\langle \mathbf{m},\mathbf{m}' \rangle_s} (\hat{s}_{\mathbf{m}}^{\dagger} \hat{s}_{\mathbf{m}'} + \text{H.c.}). \quad (14)$$

Here $U_{ss'} = \delta_{ss'} U_{xx} + (1 - \delta_{ss'}) U_{xy}$ with U_{xx} and U_{xy} given by Eqs. (10) and (13) with $v_{0x} = v_{0y} = v_{0z}$.

D. Z_2 gauge symmetry

Because of overall number conservation the Hamiltonian has the usual global U(1) symmetry. However, because the flavor conversion occurs pairwise and locally (i.e., on site), the Hamiltonians described above also exhibit an infinite number of Z_2-gauge symmetries corresponding to conservation modulo 2 of the number of X particles in any given column of the lattice running in the x direction (and similarly for Y and Z particles). These symmetries correspond to invariance under each of the transformations

$$U_X^{(m_y,m_z)} = \exp\left(i\pi \sum_{m_x} \hat{X}^{\dagger}_{(m_x,m_y,m_z)} \hat{X}_{(m_x,m_y,m_z)} \right),$$

$$U_Y^{(m_x,m_z)} = \exp\left(i\pi \sum_{m_y} \hat{Y}^{\dagger}_{(m_x,m_y,m_z)} \hat{Y}_{(m_x,m_y,m_z)} \right),$$

$$U_Z^{(m_x,m_y)} = \exp\left(i\pi \sum_{m_z} \hat{Z}^{\dagger}_{(m_x,m_y,m_z)} \hat{Z}_{(m_x,m_y,m_z)} \right),$$

where the integer pair (m_i, m_j) in the superscript of each U determines the location of a column. The first transformation for example takes $\hat{X}_{(m_x,m_y,m_z)} \to -\hat{X}_{(m_x,m_y,m_z)}$ for all m_x in the column specified by m_y and m_z. Since $\hat{X}^{\dagger}$ and $\hat{X}$ operators always appear pairwise, the Hamiltonian is invariant under this class of Z_2 transformations. These Z_2 symmetries are in a sense intermediate between local and global. While the number of such symmetries is infinite (in the thermodynamic limit) it is of course subextensive and thus not large enough to fully constrain the system (or to make it integrable for example). As mentioned in the Introduction, such symmetries have been found in certain frustrated spin models [21–24] and in a Bose metal model [25] and are known to cause dimensional reduction in some cases [21,22,24]. Because introducing a defect across which the sign of the Z_2 order parameter changes along any given single column costs only finite energy, the system will, like the 1D Ising model, disorder at any finite temperature, thereby restoring the Z_2 symmetry. We will see below how this reduced-dimensionality physics appears in a simple way in this system.

IV. MEAN-FIELD-THEORY PHASE DIAGRAMS FOR THE EFFECTIVE HAMILTONIANS

Having derived effective Hamiltonians in one, two, and three dimensions, we turn now to the investigation of their ground states. The 1D, single-flavor Hamiltonian has been extensively studied (see for instance Ref. [39] and references therein) and needs no further discussion here. The other two Hamiltonians in Eqs. (12) and (14) deserve some attention though.

A. Phase diagram in 2D, two flavors

The 2D Hamiltonian (12) is a two-flavor bosonic Hubbard Hamiltonian, a system that has recently received much attention and has been shown to have a rich phase diagram [14–18,40]. In this section we will investigate the ground state of the Hamiltonian in Eq. (12) using simple mean-field theory. The Hamiltonian (12) differs from those previously studied in two aspects: the presence of pairwise interflavor mixing and the anisotropic tunneling.

We follow here the method suggested in Ref. [41] (see also Refs. [9,10]). We consider the possibility that the global U(1) and columnar Z_2 symmetries discussed in Sec. III D are spontaneously broken by introducing complex scalar columnar order parameter fields $\psi_x(m_y)$ and $\psi_y(m_x)$, i.e., one for each x column and one for each y column. These fields should then satisfy the self-consistency conditions

$$\psi_x(m_y) = \langle \hat{X}_{(m_x,m_y)} \rangle \quad (15)$$

for all m_x in the x column specified by m_y, and,

$$\psi_y(m_x) = \langle \hat{Y}_{(m_x,m_y)} \rangle \quad (16)$$

for each m_y in the y column specified by m_x. For simplicity we omit in this discussion of the 2D (two-flavor) case the z component m_z of the position vector $\mathbf{m}$. The possibility that fluctuations restore the symmetry will be discussed further below.

Mean-field theory results from decoupling sites in the same column by neglecting fluctuations in the kinetic energy. For instance, for the x column specified by a particular value of m_y one has

$$\begin{aligned} \hat{X}^{\dagger}_{(m_x,m_y)} \hat{X}_{(m_x+1,m_y)} &= [\hat{X}^{\dagger}_{(m_x,m_y)} - \psi_x^*(m_y) + \psi_x^*(m_y)] \\ &\quad \times [\hat{X}_{(m_x+1,m_y)} - \psi_x(m_y) + \psi_x(m_y)] \\ &\approx \psi_x(m_y) \hat{X}^{\dagger}_{(m_x,m_y)} + \psi_x^*(m_y) \hat{X}_{(m_x+1,m_y)} \\ &\quad - |\psi_x(m_y)|^2. \end{aligned}$$

Thus the sites along each column decouple. Doing the same for the Y's and writing the Hamiltonian in dimensionless form where all energies are scaled by U_{xx}, i.e., $h_{2D} \equiv H_{2D}/U_{xx}$, $\tilde{t} \equiv t/U_{xx}$, and $\tilde{U}_{xy} \equiv U_{xy}/U_{xx}$, we obtain $h_{2D} \approx \sum_{\mathbf{m}} h_{2D}^{MF}(\mathbf{m}; \psi_x(m_y), \psi_y(m_x))$. Here, the on-site mean-field Hamiltonians are given by

$$\begin{aligned} h_{2D}^{MF}(\mathbf{m}; \psi_x(m_y), \psi_y(m_x)) &= -2\tilde{t} [\psi_x(m_y) \hat{X}^{\dagger}_{\mathbf{m}} + \psi_x^*(m_y) \hat{X}_{\mathbf{m}}] - 2\tilde{t} [\psi_y(m_x) \hat{Y}^{\dagger}_{\mathbf{m}} \\ &\quad + \psi_y^*(m_x) \hat{Y}_{\mathbf{m}}] + \tilde{U}_{xy} \hat{n}_{\mathbf{m}}^{(x)} \hat{n}_{\mathbf{m}}^{(y)} \end{aligned}$$

$$+\sum_{s=x,y}\left(\frac{1}{2}\hat{n}_{\mathbf{m}}^{(s)}(\hat{n}_{\mathbf{m}}^{(s)}-1)-\tilde{\mu}\hat{n}_{\mathbf{m}}^{(s)}+2\tilde{t}|\psi_s(\mathbf{m})|^2\right)$$

$$+\frac{\tilde{U}_{xy}}{2}(\hat{X}_{\mathbf{m}}^{\dagger}\hat{X}_{\mathbf{m}}^{\dagger}\hat{Y}_{\mathbf{m}}\hat{Y}_{\mathbf{m}}+\hat{Y}_{\mathbf{m}}^{\dagger}\hat{Y}_{\mathbf{m}}^{\dagger}\hat{X}_{\mathbf{m}}\hat{X}_{\mathbf{m}}],\qquad(17)$$

where $\tilde{\mu}\equiv\mu/U_{xx}$ serves as a common chemical potential. The on-site Hamiltonians satisfy the eigenvalue relations

$$h_{2D}^{MF}(\mathbf{m};\psi_x,\psi_y)|\epsilon_n(\psi_x,\psi_y)\rangle=\epsilon_n(\psi_x,\psi_y)|\epsilon_n(\psi_x,\psi_y)\rangle$$

for two arbitrary complex fields. An eigenstate of the full mean-field Hamiltonian can be written as a product state of such eigenstates,

$$|\Psi\rangle=\prod_{\mathbf{m}}|\epsilon_{n_{\mathbf{m}}}(\psi_x(m_y),\psi_y(m_x))\rangle$$

where the fields satisfy the self-consistency conditions in Eqs. (15) and (16). The mean-field ground state is obtained by globally minimizing the energy

$$E=\sum_{\mathbf{m}}\epsilon_{n_{\mathbf{m}}}(\psi_x(m_y),\psi_y(m_x))$$

with respect to the fields and the set of eigenstates $\{n_{\mathbf{m}}\}$. This is most easily done by numerical diagonalization in a truncated Hilbert space where each site can hold at most a total of $N_{\max}$ atoms. Since

$$\min_{[n_{\mathbf{m}},\psi_x(m_y),\psi_y(m_x)]}\left(\sum_{\mathbf{m}}\epsilon_{n_{\mathbf{m}}}(\psi_x(m_y),\psi_y(m_x))\right)$$

$$\geqslant\sum_{\mathbf{m}}\min_{(n,\psi_x,\psi_y)}\epsilon_n(\psi_x,\psi_y),$$

it is enough to minimize the ground-state energy of a single site with respect to the fields and then find the largest manifold of states compatible with having columnar order parameters fields. Carrying out this scheme reveals two different scenarios for the minimum of each on-site energy $\epsilon_n(\psi_x,\psi_y)$; either $\psi_x=\psi_y=0$ and n_x+n_y is integer (incompressible), or $|\psi_x|=|\psi_y|\neq 0$ (compressible). The former case corresponds to a Mott insulating state while the latter suggests a superfluid phase.

Due to the positivity of U_{xy} the last term in the mean-field Hamiltonian is minimal whenever ψ_x and ψ_y, on the same site, have a phase difference of $\pm\pi/2$.

For the (mean-field) ground-state manifold we must have in this phase $|\psi_x(m_y)|=|\psi_y(m_x)|$ for all x- and y-column order parameters. Requiring the phases of all ψ_x in each x and all ψ_y in each y column to be the same while fixing the relative phase between ψ_x and ψ_y to $\pm\pi/2$ results in configurations as the one shown in Fig. 5. Here the phases of ψ_x and ψ_y are shown represented as arrows (planar spins). The direction of the arrows defines the angle. Clearly, this phase shows a breaking of the global U(1) symmetry. The meaning of the quasilocal nature of the Z_2 symmetries discussed above becomes clear. Although the phases of ψ_x in each x column are the same there is no energy cost associated with flipping all the x spins in a single x column or all the y spins in a y column. The ordering between different columns is thus nematic.

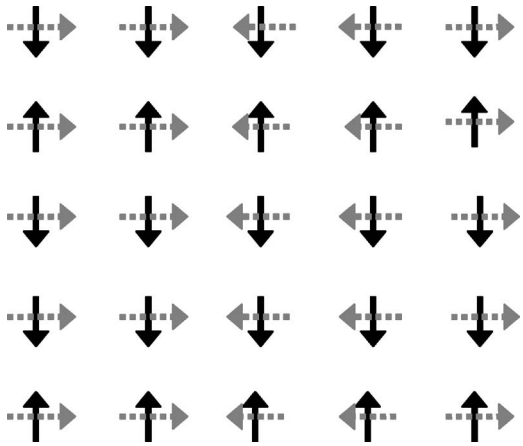

FIG. 5. Columnar phase ordering in 2D superfluid phase. The directions of the arrows correspond to the phase angles $\phi_x(m_y)$ and $\phi_y(m_x)$ of the order parameter fields $\psi_x(m_y)=|\psi_x(m_y)|e^{i\phi_x(m_y)}$ and $\psi_y(m_x)=|\psi_y(m_x)|e^{i\phi_y(m_x)}$. Solid arrows correspond to ϕ_x and dashed to ϕ_y.

One should note here that since the only energy cost associated with flipping a single spin, say an x spin in an x column, is given by the states of the neighboring x spins in the column, the situation is essentially that of a 1D Ising model along each column. Hence, at any finite temperature, domains of flipped spins will proliferate and the Z_2 symmetries will be restored. This essentially one-dimensional behavior is an example of the dimensional reduction mentioned above.

The model under consideration is highly anisotropic. Mainly since X particles can hop only in the x direction, it seems to be impossible to develop phase coherence among X particles in different x columns (and similarly for the other flavors). Suppose, however, that, as discussed above, the flavor exchange interaction term causes the relative phase of two flavors, say X and Y, to lock together so that $\hat{Y}^{\dagger}\hat{X}$ condenses,

$$\psi\equiv\langle\hat{Y}^{\dagger}\hat{X}\rangle\neq 0.$$

In this case the mean-field decomposition of the exchange interaction yields terms of the form

$$V\sim\psi\hat{Y}^{\dagger}\hat{X}+\psi^{*}\hat{X}^{\dagger}\hat{Y}$$

which permit individual particles to change flavor, and hence phase coherence can freely propagate in all directions throughout the lattice via a kind of "Andreev" process (i.e., the self-energy is off diagonal in flavor index) in which an X particle can turn into a Y particle when it needs to travel in the y direction.

To understand this isotropic superfluid phase, it is convenient to consider a phase-only representation with compact phase variables on each site $\hat{X}_{\mathbf{m}}\rightarrow e^{-i\varphi_{\mathbf{m}}^{x}}$ and $\hat{Y}_{\mathbf{m}}\rightarrow e^{-i\varphi_{\mathbf{m}}^{y}}$. The flavor exchange (Josephson) term then becomes [for the 2D (two-flavor) case]

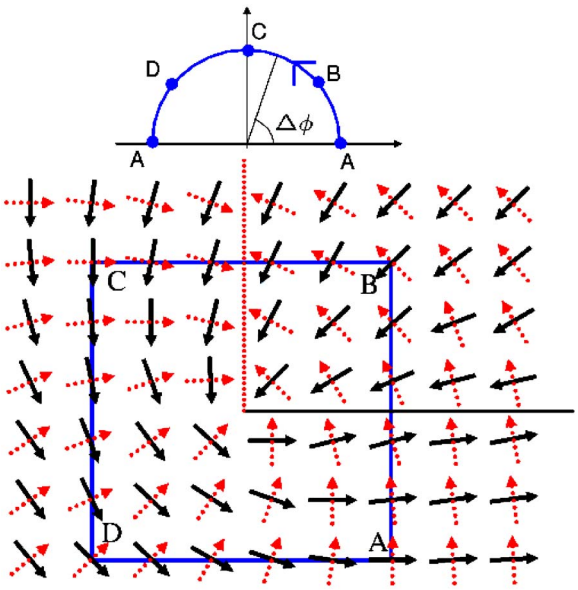

FIG. 6. (Color online) Phase configuration for ψ_x [(black) solid arrows] and ψ_y [(red) dashed arrows] containing a half vortex. Notice the branch cuts indicated by the long solid (black) and dashed (red) lines. The Z_2 symmetry means that these branch cuts have zero "string tension" and contribute only a finite core energy to the vortex. The half winding number can be seen by going around a loop *A-B-C-D-A* and calculating the total phase twist $\Delta\phi$. This twist is calculated by summing the changes in φ^y when going vertically and φ^x when going horizontally.

$$V = \tilde{U}_{xy} \sum_{\mathbf{m}} \cos[2(\varphi^x_{\mathbf{m}} - \varphi^y_{\mathbf{m}})].$$

Defining $\varphi^{\pm}_{\mathbf{m}} \equiv \varphi^x_{\mathbf{m}} \pm \varphi^y_{\mathbf{m}}$ we have

$$V = \tilde{U}_{xy} \sum_{\mathbf{m}} \cos(2\varphi^-_{\mathbf{m}}).$$

Assuming that the relative phase of the condensates is locked together by this Josephson term is equivalent to assuming that (for $U_{xy} > 0$) the fluctuations of φ^- away from the ground-state value $\pi/2$ (or its equivalent $-\pi/2$ under the Z_2-gauge symmetry) are massive and can be ignored. Thus we obtain $\varphi^{(x,y)}_{\mathbf{m}} = \varphi^+_{\mathbf{m}}/2 \pm \pi/4$. The continuum limit of the anisotropic kinetic energy $T = (\partial_x \varphi^x)^2 + (\partial_y \varphi^y)^2$ then becomes $T \sim [(\partial_x \varphi^+)^2 + (\partial_y \varphi^+)^2]$ and we immediately see that the anisotropy has effectively disappeared at long wavelengths and we have a superfluid.

A vortex configuration in φ^+ can be viewed as a bound state of two half vortices in the φ^x and φ^y fields. The columnar Z_2 symmetry allows the ψ_x field to have a phase jump of π across a cut parallel to the x axis and similarly for ψ_y. Thus half vortices are permitted. If the two order parameter phases are locked together (φ^- fluctuations are massive) then the two half vortices are confined to each other as shown in Fig. 6. Such a vortex has an energy which scales (as usual) only logarithmically with system size, despite the semi-infinite branch cut (π phase jump) of ψ_x running horizontally out to the right from the vortex center and of the similar branch cut in ψ_y running vertically out above the vortex center. To see that such a vortex is topologically well defined despite the Z_2 symmetry one can consider a loop around the vortex core as shown in Fig. 6. In going around the loop we add up the phase twist $\Delta\phi$ and map onto the complex plane. To calculate $\Delta\phi$ along the loop the changes in φ^y have to be added when going vertically and the changes in φ^x when going horizontally. The net result is that going once around the vortex core the phase winds by π. If one applies a π flip in all the φ^x (φ^y) phases in any row (column) the mapping onto the complex plane remains invariant.

The Mott insulating states, having integer number of atoms in each well, are best characterized by the $\tilde{t}=0$ eigenstates. These are product states

$$|\Psi_0(\tilde{t}=0)\rangle = \prod_{\mathbf{m}} |\psi_{Ni}(\mathbf{m})\rangle,$$

where $h^{MF}_{2D}(0,0)|\psi_{Ni}\rangle = \epsilon_{Ni}|\psi_{Ni}\rangle$ and the integer N is the total number of particles $N = n_x + n_y$ in each well. The index i runs from 0 to N for each N and for the three lowest values of N the eigenstates are

$$|\psi_{00}\rangle = |0\rangle, \quad \epsilon_{00} = 0,$$

$$|\psi_{10}\rangle = |1_x, 0_y\rangle, \quad \epsilon_{10} = -\tilde{\mu},$$

$$|\psi_{11}\rangle = |0_x, 1_y\rangle, \quad \epsilon_{11} = -\tilde{\mu},$$

$$|\psi_{20}\rangle = |1_x, 1_y\rangle, \quad \epsilon_{20} = -2\tilde{\mu} + \tilde{U}_{xy},$$

$$|\psi_{21}\rangle = \frac{1}{\sqrt{2}}(|2_x, 0_y\rangle + |0_x, 2_y\rangle), \quad \epsilon_{21} = 1 - \tilde{U}_{xy} - 2\tilde{\mu},$$

$$|\psi_{22}\rangle = \frac{1}{\sqrt{2}}(|2_x, 0_y\rangle - |0_x, 2_y\rangle), \quad \epsilon_{22} = 1 + \tilde{U}_{xy} - 2\tilde{\mu}.$$

In Fig. 7 the mean-field phase diagram has been drawn for the physically relevant value $\tilde{U}_{xy} = 1/3$ which is characteristic for the proposed setup. The lobes marked MI correspond to incompressible Mott insulating phases with integer filling factors. The remaining part of the diagram, marked SF, corresponds to a superfluid phase with the columnar nematic ordering (see Fig. 5) discussed above. Considering the $t=0$ eigenstates above two things become clear. Trivially, if $\tilde{U}_{xy} \to 0$ the lowest lobe, and all other odd filling lobes, vanish and the model reduces to two noninteracting single-flavor models as expected. Second, at $\tilde{U}_{xy} = 0.5$ there is a level crossing between $|\psi_{20}\rangle$ and $|\psi_{21}\rangle$. It follows that the size of the lowest odd filling lobes increases with increasing values of $\tilde{U}_{xy}$ up until $\tilde{U}_{xy} = 0.5$ after which it starts to decrease again.

By considering fluctuation effects higher order in the tunneling amplitude, we can demonstrate that the permutational symmetry between the X and Y flavors can be broken in the Mott insulator phase. In the absence of tunneling, the single-particle states $|\psi_{10}\rangle$ and $|\psi_{11}\rangle$ are degenerate. Taking tunneling into account breaks this degeneracy and to second order in $\tilde{t}$ (using for instance the Schrieffer-Wolff transformation

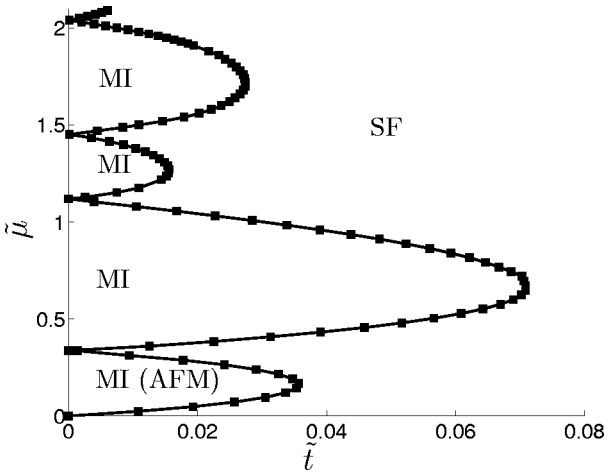

FIG. 7. Mean-field ground-state phase diagram for the 2D (two-flavor) Hamiltonian in Eq. (17) in the plane of $\tilde{\mu}$, the scaled chemical potential μ/U_{xx}, and $\tilde{t}=t/U_{xx}$, the scaled hopping energy, here calculated for the experimentally relevant ratio $\tilde{U}_{xy}\equiv U_{xy}/U_{xx}=1/3$ using a truncated Hilbert space with at most ten particles per site. Lobes of Mott insulating states, of successively increasing integer filling factor with increasing chemical potential $\tilde{\mu}$, are surrounded by a superfluid phase. The superfluid phase is characterized by columnar order parameter fields $\psi_x(m_y)$ and $\psi_y(m_x)$, one for each x and y column, respectively. All ψ_x and ψ_y have equal, nonzero, magnitudes while their relative phases are either 0 or π (see Fig. 5).

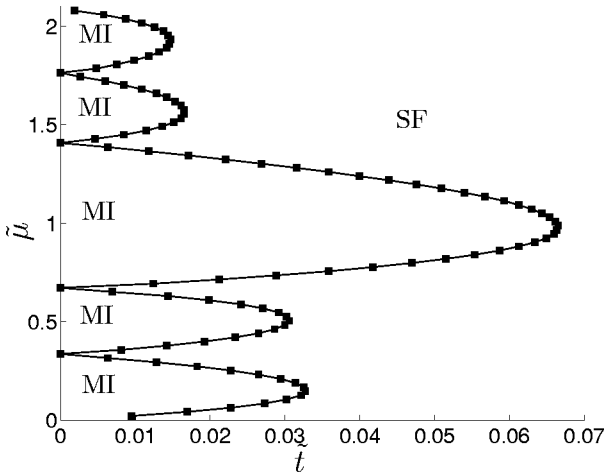

FIG. 8. Mean-field ground-state phase diagram for the 3D (three-flavor) Hamiltonian.

[42]) an effective (pseudo)spin-1/2 Hamiltonian for the interaction between neighboring sites can be found:

$$H_{eff}=-J_{eff}\sum_{\langle \mathbf{m},\mathbf{m}'\rangle}\hat{\sigma}^{(z)}_{\mathbf{m}}\hat{\sigma}^{(z)}_{\mathbf{m}'}. \tag{18}$$

The up and down states of the pseudospin operators $\hat{\sigma}^{(z)}_{\mathbf{m}}$ correspond to the site $\mathbf{m}$ being occupied by one X atom or one Y atom, respectively. The effective magnetic interaction is

$$J_{eff}=\frac{\tilde{t}^2(\tilde{U}^2_{xy}+2\tilde{U}_{xy}-1)}{\tilde{U}_{xy}(1-\tilde{U}^2_{xy})}.$$

There is a critical value of the interflavor interaction $\tilde{U}^c_{xy}=\sqrt{2}-1\approx 0.414$ for which J_{eff} vanishes. For $\tilde{U}_{xy}>\tilde{U}^c_{xy}$, the system is ferromagnetic and spontaneously favors one flavor over the other. For $\tilde{U}_{xy}<\tilde{U}^c_{xy}$ the system is antiferromagnetic and favors an ordering with X and Y atoms on alternating sites. Thus, we conclude that at integer filling factor the permutational symmetry between X and Y flavors (or equivalently, the cubic symmetry of the underlying lattice) is always broken in the mean-field ground state. Further, in the antiferromagnetic state, sublattice (i.e., translation) symmetry is broken as well.

B. Phase diagram in 3D, three flavors

Using the same type of mean-field theory as for the 2D (two-flavor) case, the 3D (three-flavor) case can be treated as well. The resulting phase diagram for $\tilde{U}_{xy}=1/3$ is shown in Fig. 8. Again, Mott lobes with integer filling factors are seen surrounded by a superfluid phase where all order parameters $\psi_{x,y,z}$ have equal magnitude, i.e., $|\psi_x|=|\psi_y|=|\psi_z|\neq 0$. Due to the positivity of the coefficient U_{xy} in the Josephson term in Eq. (14) the relative phases of the three condensates are frustrated (see Fig. 9). Thus writing $\psi_s=|\psi_s|e^{i\phi_s}$, $s=x$, y, z, one finds $\phi_x-\phi_y=\phi_y-\phi_z=\phi_z-\phi_x=\pm 2\pi/3\pm\pi$.

An interesting effect here is that the on-site frustrated phase configurations come in two different "chiralities" that cannot be converted into each other by shifting any one of the phases by the π shift allowed by the Z_2-gauge symmetry. To see this one may consider the current flowing between the

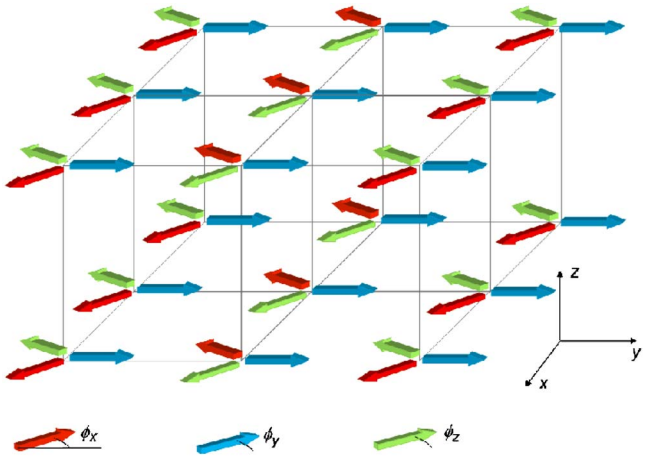

FIG. 9. (Color online) Phase ordering in 3D superfluid phase. The directions of the arrows correspond to the phase angles $\phi_x(m_y,m_z)$, $\phi_y(m_x,m_z)$, and $\phi_z(m_x,m_y)$ of the order parameter fields $\psi_x(m_y,m_z)=|\psi_x(m_y,m_z)|e^{i\phi_x(m_y,m_z)}$, $\psi_y(m_x,m_z)=|\psi_y(m_x,m_z)|e^{i\phi_y(m_x,m_z)}$, and $\psi_z(m_x,m_y)=|\psi_y(m_x,m_y)|e^{i\phi_y(m_x,m_y)}$. As in the 2D (two-flavor) case the underlying symmetry of the Hamiltonian allows for flipping, say, all the ϕ_x along any x column by π to obtain another ground-state configuration. In addition to the ground-state degeneracy obtained from such operations, an accidental degeneracy associated with parallel planes of different chirality is present. In this figure the middle x-z plane has a different chirality from the other two x-z planes.

condensates of different flavors on a given site. The current flowing between the X and Y condensates on a particular site is determined by $\sin[2(\phi_x-\phi_y)]$. In a right-handed configuration with, say, $\phi_x=0$, $\phi_y=2\pi/3$, $\phi_z=4\pi/3$ there is an on-site current flowing from

$$X \to Y \to Z \to X.$$

The situation is different in a left-handed configuration with $\phi_x=0$, $\phi_y=4\pi/3$, $\phi_z=2\pi/3$, where the current is now flowing in the opposite direction, i.e.,

$$X \leftarrow Y \leftarrow Z \leftarrow X.$$

Adding an arbitrary phase of π (i.e., invoking the Z_2 symmetry) to any of the phases does not affect these currents.

Starting from a ground state with the same chirality throughout the system one can choose a set of parallel planes and change the chirality of each plane individually. Such changing of chirality of a plane requires that the whole plane has the same chirality. This additional ground-state degeneracy is not associated with any symmetry of the Hamiltonian but is an accidental one. A similar situation occurs for special parameter values in frustrated XY models, where parallel zero-energy domain walls can be inserted [28]. One should note that such accidental degeneracies at the mean-field level may be lifted by fluctuation effects associated with collective modes such as spin waves.

As in the 2D (two-flavor) case, the smaller Mott lobes, corresponding to integer filling factors not divisible by the dimensionality of the system, are degenerate in the $\tilde{t}=0$ limit. This degeneracy is lifted due to tunneling, leading to (pseudo)magnetic ordering like that demonstrated for the 2D (two-flavor) case. To fully lift the degeneracy one has to employ fourth-order perturbation theory. The resulting Hamiltonian will include terms acting simultaneously on three and four sites. However, such fourth-order corrections are very small and may be difficult to observe in the proposed experimental situation. They can, however, lead to novel physics and can be intentionally generated [43,44].

Before leaving this section, we comment on the possibility of breaking the permutational symmetry among the flavors in the superfluid phase. As is well known, large interspecies interaction strength in the two flavor bosonic Hubbard model leads to phase separation. A phenomena occurring also here if $\tilde{U}_{xy} \geqslant 0.5$. However, due to the positive constant in front of the "Josephson" (flavor changing) term, another phenomenon can take place in the 3D (three flavors) model.

As an example consider Fig. 10. Here $\tilde{\mu}=0.27$ and $\tilde{U}_{xy}=0.8$. As can be seen for small $\tilde{t}$ the system is in a Mott insulating state with filling factor 2. As t increases the system becomes superfluid. This occurs in two steps. First, mean-field theory predicts a second-order transition to a state with only one flavor superfluid and then a first-order transition to a state with two nonzero superfluid order parameters of equal magnitude. Increasing the hopping strength further does not seem to make the third flavor superfluid. We attribute this to the large energy cost associated with having the phases of the three order parameters in a frustrated configuration.

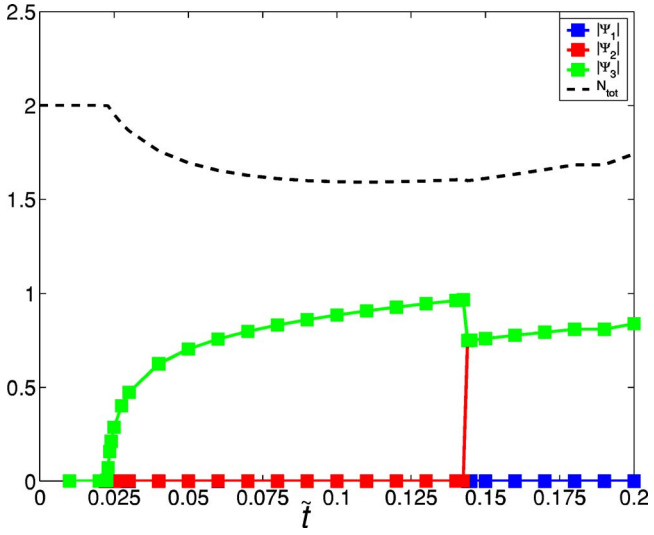

FIG. 10. (Color online) Example of broken permutational symmetry. If one increases the interspecies interaction $\tilde{U}_{xy}$ beyond 1/3, superfluid phases with broken permutational symmetry can be achieved. Shown here are the order parameters sorted according to magnitude, $\Psi_1=\max(\psi_x,\psi_y,\psi_z)$, $\Psi_3=\min(\psi_x,\psi_y,\psi_z)$ for an interspecies interaction $\tilde{U}_{xy}=0.8$ as a function of $\tilde{t}$. The total number of particles is shown as a dashed line.

V. INTERFERENCE PATTERNS AND DENSITY CORRELATIONS

The traditional way of detecting superfluidity is by releasing the trap and looking at the density distribution of the expanding cloud. Provided that the cloud expands many times its initial diameter, the final position of a particle is determined by its momentum rather than its initial position. Hence this expanded real-space density distribution provides a direct picture of the momentum-space distribution of the trapped system. More precisely, the density distribution a time t after trap release is related to the momentum density of the trapped state $|\Phi\rangle$ as

$$\langle n(\mathbf{r},t)\rangle = \left(\frac{m}{ht}\right)^3 \langle\Phi|n_{\mathbf{Q}(\mathbf{r})}|\Phi\rangle$$

where $\mathbf{Q}(\mathbf{r})=m\mathbf{r}/(\hbar t)$. It is useful to think of this spatial distribution as resulting from interference of matter waves radiated by the different lattice sites when the trap is released. The one-dimensional character of the Z_2-gauge symmetry means that thermal fluctuations can destroy the long-range phase order by allowing the phase on an arbitrary site to flip by $\pm\pi$. If the system disorders in this way, any interference pattern in the radiated matter waves will be destroyed as well. In this case, further information about the correlations in the system can be obtained by looking at the density fluctuations (noise) in the released cloud [45–47] in a Hanbury-Brown-Twiss- (HBT-)like statistical measurement.

We begin this section by looking at the zero-temperature momentum distribution and then consider the density fluctuations of the expanded cloud around its mean.

A. Interference patterns

Although any real experiment is conducted at finite temperature, the zero-temperature columnar phase ordering may prevail for a finite system at low enough temperatures. The zero-temperature momentum distribution is thus of interest and we will estimate it by using a single macroscopically occupied wave function corresponding to the superfluid states in the two- and three-flavor cases. The details of the calculations can be found in the Appendix and we here only state the main results.

We begin by considering a single 2D plane with $N\times N$ sites at zero temperature in the two-flavor system and model the superfluid state with a macroscopically occupied wave function

$$|\Phi\rangle = \frac{(a_{SF}^{\dagger})^M}{\sqrt{M!}}|0\rangle.$$

Here $|0\rangle$ is the vacuum state of the lattice, i.e., no atoms present, while $a_{SF}^{\dagger}$ is the creation operator

$$a_{SF}^{\dagger} \equiv \frac{1}{\sqrt{2N}}\sum_{m=1}^{N}\sum_{n=1}^{N}(\alpha_{mn}X_{mn}^{\dagger} + \beta_{mn}Y_{mn}^{\dagger}).$$

The subscripts m and n denote the coordinates, rows and columns, in the lattice while α and β are phase factors ($|\alpha| = |\beta| = 1$) determining the phase of the wave function on a given site. At zero temperature the phases of X particles are ordered along rows while the phases of Y particles are ordered along columns, i.e., $\alpha_{mn}=\alpha_m$ and $\beta_{mn}=\beta_n$ (cf. Figs. 5 and 17). For a macroscopic occupation M the observed density distribution in a single shot in the x-y plane after expansion is proportional to the momentum distribution $\langle\Phi|\psi_{\mathbf{Q}}^{\dagger}\psi_{\mathbf{Q}}|\Phi\rangle$. As shown in the Appendix we have for a single 2D plane in the two-flavor system

$$\langle\Phi|\psi_{\mathbf{Q}}^{\dagger}\psi_{\mathbf{Q}}|\Phi\rangle = |\tilde{\Psi}_x(\mathbf{Q})|^2 + |\tilde{\Psi}_y(\mathbf{Q})|^2$$

where

$$|\tilde{\Psi}_x|^2 = \pi M|\tilde{\phi}_0^x(\mathbf{Q})|^2 f_1(Q_y,\alpha_m)\sum_{\text{odd } n}\delta(aQ_x - n\pi),$$

$$|\tilde{\Psi}_y|^2 = \pi M|\tilde{\phi}_0^y(\mathbf{Q})|^2 f_1(Q_x,\beta_n)\sum_{\text{odd } m}\delta(aQ_y - m\pi).$$

The functions $\tilde{\phi}_0^x$ and $\tilde{\phi}_0^y$ are the Fourier transforms of the on-site Wannier functions and $f_1(Q_y,\alpha_m)$ and $f_1(Q_x,\beta_n)$ are $2\pi/a$-periodic random functions with typical magnitude of order unity which depend on which of the degenerate ground states is observed (see Fig. 18 and the Appendix for details). From the above equations the interference pattern from a single 2D plane in the two-flavor system can be seen to be a gridlike structure as shown in Fig. 11 where the interference pattern has been calculated numerically for a 40×40 lattice. The appearance of lines, rather than points as in a single-flavor 2D system, stems from the one-dimensional character of the superfluid state with phases being aligned only along rows (columns) but randomly distributed between rows (columns). The randomness in the distribution between the rows (columns) shows up as the random interference pattern along grid lines.

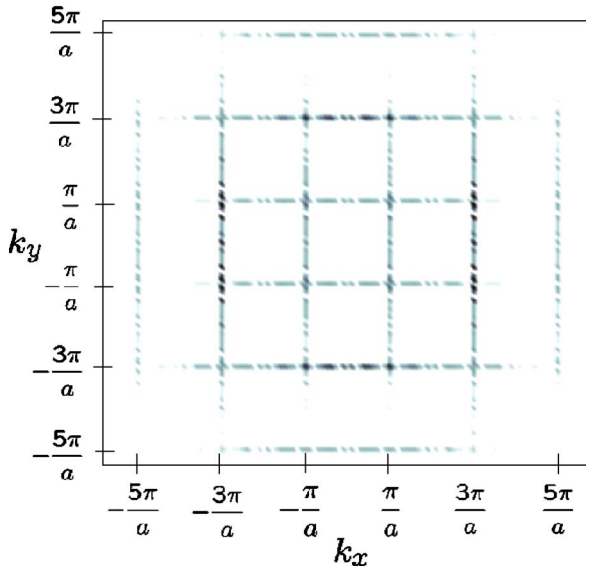

FIG. 11. (Color online) Calculated momentum distribution for a 40×40 lattice. The momentum distribution was calculated by numerically summing the contributions to the distribution function.

In an experiment one typically does not probe a single plane, but it is the integrated density of a large number of planes that is imaged. For imaging in the plane parallel to the 2D planes the integrated column density (intensity in the absorption image) is for an $N\times N\times N$ lattice with M atoms in each 2D plane

$$I(Q_x,Q_y) = N\int\frac{dQ_z}{2\pi}\overline{\langle\Phi|\psi_{\mathbf{Q}}^{\dagger}\psi_{\mathbf{Q}}|\Phi\rangle}.$$

Here the bar over the quantum-mechanical averaging denotes the averaging over the different ground-state configurations allowed by the Z_2 symmetry. Since $\overline{f_1(Q,\alpha_m)}=1$ (see Appendix) the random interferences seen in Fig. 11 will be averaged out and a grid of smooth lines, void of interference, will be seen. Another source of smoothing out the random interferences comes from limited detector precision. For a large system, the random oscillations becomes increasingly rapid and only an average over nearby momenta can be probed.

In the 3D (i.e., three-flavor) case, the situation is very similar. Special care has to be taken with accidental symmetry breaking of the ground state giving rise to planes of different chirality. If we assume that planes with uniform chirality have normals in the x direction the momentum distribution can be written

$$\begin{aligned}\langle\Phi|\psi_{\mathbf{Q}}^{\dagger}\psi_{\mathbf{Q}}|\Phi\rangle = {} & |\tilde{\Psi}_x(\mathbf{Q})|^2 + |\tilde{\Psi}_y(\mathbf{Q})|^2 + |\tilde{\Psi}_z(\mathbf{Q})|^2 \\ & + 2\,\mathrm{Re}[\tilde{\Psi}_x(\mathbf{Q})^*\tilde{\Psi}_y(\mathbf{Q})] \\ & + 2\,\mathrm{Re}[\tilde{\Psi}_y(\mathbf{Q})^*\tilde{\Psi}_z(\mathbf{Q})] + 2\,\mathrm{Re}[\tilde{\Psi}_z(\mathbf{Q})^*\tilde{\Psi}_x(\mathbf{Q})]\end{aligned} \tag{19}$$

where

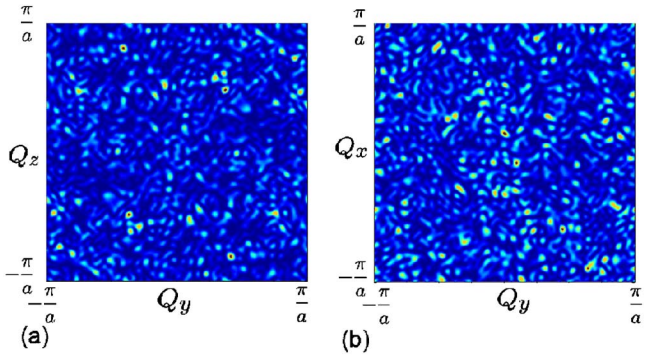

FIG. 12. (Color online) (a) The random function $f_2(Q_y, Q_z, \eta^x_{no})$ for a 40×40 lattice for a specific realization of η^x_{no}. Note that f_2 is symmetric under inversion. (b) The random function $g^y_2(Q_x, Q_z, \eta^y_{no}, \sigma_m)$ for a 40×40 lattice for a specific realization of η^y_{no} and σ_m. Note that g_2 is not symmetric under inversion.

$$|\tilde{\Psi}_x|^2 = 2\pi|\tilde{\phi}^x_0|^2\frac{M}{3}f_2(Q_y, Q_z, \eta^x_{no})\sum_{\text{odd } n}\delta(aQ_x - n\pi),$$

$$|\tilde{\Psi}_y|^2 = 2\pi|\tilde{\phi}^y_0|^2\frac{M}{3}g^y_2(Q_z, Q_x, \eta^y_m, \sigma_m)\sum_{\text{odd } n}\delta(aQ_y - n\pi),$$

$$|\tilde{\Psi}_z|^2 = 2\pi|\tilde{\phi}^z_0|^2\frac{M}{3}g^z_2(Q_x, Q_y, \eta^z_m, \sigma_m)\sum_{\text{odd } n}\delta(aQ_z - n\pi).$$

Again, since long-range order is aligned only along 1D strips, the released cloud will be a set of intersecting perpendicular planes with intersections at positions corresponding to odd momenta $Q_{x,y,z}=(2n+1)\pi/a$. The planes in each direction will have a random intensity modulation specified by the random functions f_2, g^y_2, and g^z_2 (see the Appendix for details). Examples of these distribution functions f_2 and g_2 are shown in Fig. 12. The last three terms in Eq. (19) randomly modulate the distribution along the intersections of the planes.

If a single-shot measurement is made, the integrated column density will show a pattern of grid lines similar to that in Fig. 11, the grid lines showing random interference patterns. Between the lines a periodic random distribution (of lesser intensity than the lines) will be present. This latter distribution will be either f_2 or g_2 depending on the orientation of the planes with uniform chirality. Thus if the absorbtion image is taken in the same plane as the planes with uniform chirality this background modulation will be symmetric under space inversion [cf. Fig. 12(a)] whereas if it is taken perpendicular there will be no such symmetry in the random modulation [cf. Fig. 12(b)].

B. Density-density correlations

As pointed out above, the dimensional reduction present in the system means that finite temperatures can destroy the 1D Ising-like ordering of phases along columns and that the individual phases at any one site can be flipped $\pm\pi$, i.e., the Z_2-gauge symmetry is restored. In this case there will be no visible interference pattern although atoms are delocalized, i.e., the δ peaks will be smeared and a random density distribution will be seen for each shot.

To illustrate the usefulness of correlation measurements we consider a single $N\times N$ 2D plane in the two-flavor system at unit filling ($M=N^2$). If the temperature is finite, not only may the Z_2 symmetry in the superfluid state be restored but it is also possible for the unit filling Mott state to be disordered. There are then four different possible states the system can be in:

(1) superfluid with restored Z_2 symmetry;

(2) ferromagnetic Mott insulator (all atoms of the same flavor);

(3) antiferromagnetic Mott insulator (alternating flavors on alternating sites); and

(4) disorder Mott insulator (each site having one atom but with random flavor).

If one makes multiple single-shot measurements and averages the density distribution obtained in each shot, one obtains a measure of the average momentum distribution (see the Appendix)

$$\overline{\langle\Phi|n_{\mathbf{Q}}|\Phi\rangle} = \frac{M}{2}[|\tilde{\phi}^x_0(\mathbf{Q})|^2 + |\tilde{\phi}^y_0(\mathbf{Q})|^2]$$

which is the same for each of the four states 1–4. We will henceforth refer to averages $\overline{\langle\cdot\rangle}$ as *disorder averages*. To distinguish the four states one can instead measure the HBT-like density-density correlations of the expanding cloud [45–47],

$$G(\mathbf{r},\mathbf{r}') \equiv \overline{\langle n(\mathbf{r})n(\mathbf{r}')\rangle_t} - \overline{\langle n(\mathbf{r})\rangle_t}\,\overline{\langle n(\mathbf{r}')\rangle_t}.$$

Here $\overline{\langle n(\mathbf{r})\rangle_t}$ is the density of atoms at point $\mathbf{r}$ a time t after the trap has been switched off averaged over many experimental realizations (see the Appendix). To measure $\overline{\langle n(\mathbf{r})n(\mathbf{r}')\rangle_t}$ one calculates the product of the observed densities $n(\mathbf{r})n(\mathbf{r}')$ in each shot and averages over several experimental runs. Just as for the density distribution, the correlation function G provides a measure of the momentum correlations,

$$G(\mathbf{r},\mathbf{r}') = \left(\frac{m}{ht}\right)^6[\overline{\langle n_{\mathbf{Q}}n_{\mathbf{Q}'}\rangle} - \overline{\langle n_{\mathbf{Q}}\rangle}\times\overline{\langle n_{\mathbf{Q}'}\rangle}],$$

prior to trap release.

To get a qualitative understanding of how the superfluid state can be detected by correlation measurements we first return to the $T=0$ result in the previous section and look at the periodic function $f_1(Q_y)$. This random modulation arose because the phases of the Y's were uncorrelated between rows. Since the relative phases of the Y's in rows is $\pm\pi$ this function is even in Q and along any given grid line the quantity $\langle n_{\mathbf{Q}}n_{\mathbf{Q}'}\rangle$ is thus strongly correlated when $Q_y+Q'_y = 2m\pi/a$. Averaging over many realizations one sees that (along a grid line of constant $Q_x=2n\pi/a$)

$$\overline{\langle n_{\mathbf{Q}}n_{\mathbf{Q}'}\rangle}_{T=0} \propto \sum_n \delta(Q_y + Q'_y - 2m\pi/a) + (\text{other terms}).$$

In the thermally disordered superfluid state the phase on any site is allowed to flip by π (restoring Z_2 symmetry). This destroys the δ peaks in $|\tilde{\Psi}_{(x,y)}|^2$ and gives instead a random

modulation given by the function $f_2(Q_x,Q_y)$. Since only π flips are allowed this modulation is symmetric $f_2(Q_x,Q_y)=f_2(-Q_x,-Q_y)$ and we get strong correlations in $\langle n_{\mathbf{Q}}n_{\mathbf{Q}'}\rangle$,

$$\overline{\langle n_{\mathbf{Q}}n_{\mathbf{Q}'}\rangle}_{T\neq 0}\propto\sum_n \delta(\mathbf{Q}+\mathbf{Q}'-\mathbf{G}_n)+(\text{other terms}),$$

where $\mathbf{G}_n$ is a reciprocal lattice vector. On a technical level (see the Appendix) this can be seen to arise since the disorder-averaged propagator for single particles is necessarily short ranged due to the random π phase changes at finite temperature, while the disorder-averaged propagators for *pairs* of particles can still be long ranged.

In the Appendix we have calculated $G(\mathbf{Q}(\mathbf{r}),\mathbf{Q}'(\mathbf{r}'))$ for the four scenarios for a single plane in the two-flavor system and we here give the qualitative results. The superfluid state is, confirming the qualitative discussion above, characterized by peaks at $\mathbf{Q}\pm\mathbf{Q}'=\mathbf{G}_n$ [see Eq. (A40)] while the ferromagnetic Mott state and the disordered Mott state have peaks only at $\mathbf{Q}-\mathbf{Q}'=\mathbf{G}_n$ [see Eqs. (A44) and (A59)]. The correlation functions in these Mott states are distinguished by having different background intensities between peaks and different peak strengths. The antiferromagnetic Mott state has peaks at half reciprocal lattice vectors $\mathbf{Q}-\mathbf{Q}'=\mathbf{G}_n/2$ [see Eq. (A51)].

In the three-flavor system the situation is similar to the two-flavor scenario discussed above. In the presence of thermal disordering of the superfluid state the interference patterns of the Mott state and the superfluid states become indistinguishable. Again, in the three-flavor case the pair propagators will be nonzero in the disordered superfluid state and $G(\mathbf{Q}(\mathbf{r}),\mathbf{Q}'(\mathbf{r}'))$ will have peaks at $\mathbf{Q}\pm\mathbf{Q}'=\mathbf{G}_n$ [see Eq. (A70)].

While there should be no problem in measuring the correlation functions for a system with three flavors, the two-flavor system poses a problem of technical nature since in an experiment several uncorrelated 2D planes will be created. Suppose one has N uncorrelated planes. If one detects one atom at position $\mathbf{r}$ and another at $\mathbf{r}'$ in a single experiment the atoms could have come from either the same plane or different planes. Measuring the product of densities in each shot and averaging over several experiments one will for the case with N 2D planes actually measure

$$N\overline{\langle n(\mathbf{r})n(\mathbf{r}')\rangle}_t+N(N-1)\overline{\langle n(\mathbf{r})\rangle}_t\overline{\langle n(\mathbf{r}')\rangle}_t$$

rather than $N\overline{\langle n(\mathbf{r})n(\mathbf{r}')\rangle}_t$. Thus the signal-to-noise ratio scales as $1/N$ requiring many experimental runs for large systems.

VI. LIFETIME ESTIMATE IN 1D

In the previous sections, effective Hamiltonians for atoms in the first band(s) of the optical lattice were introduced and the mean-field ground-state phase diagrams drawn. In doing so, it was assumed that the interaction terms in the original Hamiltonian (2) responsible for scattering particles between bands could be ignored. In this section, these interactions are taken into account perturbatively and the lifetime of atoms in the first band is estimated. The obtained (inverse) lifetime should be compared to other energy scales in the problem, most importantly the smallest one, the hopping energy. If the lifetime turns out to be long compared to the time scale of hopping, the states described in the previous sections should be possible to realize in experiment.

To simplify matters, the discussion will be restricted to the 1D case. The ensuing results are expected to agree well, both qualitatively as well as quantitatively, with the 2D and 3D cases to lowest order in perturbation theory. This follows from taking parity considerations into account when determining the allowed transitions. Thus, ignoring tunneling in the y and z directions and measuring distance in units of the lattice spacing (see Sec. II) the 1D Hamiltonian can be written $\hat{H}=\hat{H}_0+\hat{V}$ with

$$\hat{H}_0=E_R\sum_n\int d\xi\,\hat{\psi}_n^\dagger(\xi)\left(-\frac{\partial^2}{\partial\xi^2}+v_{0x}\sin^2(\xi)\right)\hat{\psi}_n(\xi)$$

and

$$\hat{V}=\frac{U}{2}\sum_{n_1,n_2,n_3,n_4}\int d\xi\,\hat{\psi}_{n_1}^\dagger(\xi)\hat{\psi}_{n_2}^\dagger(\xi)\hat{\psi}_{n_3}(\xi)\hat{\psi}_{n_4}(\xi). \quad (20)$$

Here $\hat{\psi}_n^\dagger(\xi)$ creates an atom at ξ in the nth band of the 1D system and $U\equiv 4\pi E_R(a_s/a)O_{00}(v_{0y})O_{00}(v_{0z})$.

Apart from the field operators $\hat{\psi}_n(\xi)$ it is convenient to define boson operators in two other bases. First, we have the basis of Bloch functions $u_{nk}(\xi)$ with band index n and lattice momentum k. These functions satisfy $\hat{H}_0u_{nk}(\xi)=\epsilon_n(k)u_{nk}(\xi)$ and are associated with the field operators $\hat{a}_{nk},\hat{a}_{nk}^\dagger$. Second, we have the Wannier functions $\tilde{\phi}_n(\xi-\pi m)$ defined in Sec. II. In this section we will denote the corresponding field operators by $\hat{a}_n(m),\hat{a}_n^\dagger(m)$. Note that these definitions depart from the conventions in previous sections and that operators corresponding to Bloch functions and Wannier functions are distinguished in the number of subscripts.

A. Wideband limit

We begin by looking at the case when the second term $\hat{V}$ in Eq. (20) is small compared to $\hat{H}_0$ and consider an initial state where all N atoms reside in the lowest-lying Bloch state of the first band,

$$|i\rangle=(N!)^{-1/2}(\hat{a}_{n=1,k=\pi/a}^\dagger)^N|0\rangle.$$

A first-order decay process is then one where two atoms in the first band collide, promoting one to the second band and the other to the zeroth band, i.e., the final state is

$$|f\rangle=\frac{\hat{a}_{n=2,k_2}^\dagger\hat{a}_{n=0,k_0}^\dagger\hat{a}_{n=1,k=\pi/a}\hat{a}_{n=1,k=\pi/a}}{\sqrt{N(N-1)}}|i\rangle.$$

The first-order matrix element for this transition is

$$|\langle f|\hat{V}|i\rangle|=U\delta(k_0+k_2-2m\pi/a)\sqrt{N(N-1)}\times\int u_{0k_0}^*(\xi)u_{2k_2}^*(\xi)u_{1k=\pi/a}(\xi)^2\,d\xi.$$

If the filling factor (atoms per well) of the first band is ν_1,

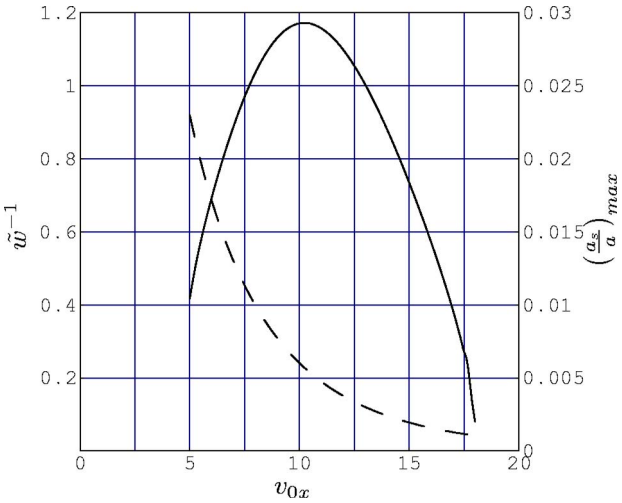

FIG. 13. (Color online) Solid line: Inverse of the coefficient $\tilde{w}$ occurring in Eq. (21) for the first-order decay rate calculated in the wideband limit. In this limit, there are no available energy states for the first-order decay provided $19 < v_{0x}$. Dashed line: The maximum value of the ratio a_s/a for which the wideband analysis is valid.

and the density of states of the nth band is $\rho(\epsilon_n(k))$ the transition rate per well becomes

$$w \approx \frac{2\pi}{\hbar} \frac{(\nu_1 U)^2 \left| \int u^*_{0k_0}(\xi) u^*_{2k_2}(\xi) u_{1k=\pi/a}(\xi)^2 d\xi \right|^2}{\rho(\epsilon_0(k_0))^{-1} + \rho(\epsilon_2(k_2))^{-1}}.$$

Defining

$$\tilde{w}(v_{0z}) \equiv \frac{32\pi^3 E_R}{\rho(\epsilon_0)^{-1} + \rho(\epsilon_2)^{-1}} \left| \int u^*_{0k_0} u^*_{2k_2} u^2_{1k=\pi/a} \, d\xi \right|^2$$

this can be compactly written as

$$w = \frac{E_R}{\hbar} \nu_1^2 \left(\frac{a_s}{a} \right)^2 O_{00}(v_{0y})^2 O_{00}(v_{0z})^2 \tilde{w}(v_{0x}). \tag{21}$$

In Fig. 13 $\tilde{w}(v)$ obtained from numerical calculation is shown. For convenience the inverse of $\tilde{w}$ has been plotted. As can be seen, the lifetime goes to zero for small and large v. This is a result of the diverging density of states at the band edges. Above $v \approx 19$ the first-order process is no longer energetically possible and higher-order perturbation theory has to be applied.

The validity of the wideband calculation relies upon the assumption that the inequality $\nu_1 U < t$ is satisfied. This condition can be used to obtain an upper bound on the ratio a_s/a by assuming the lattice depth to be the same in all directions, i.e., $v_{0x} = v_{0y} = v_{0z} = v_0$, which yields

$$\frac{a_s}{a} < \left(\frac{a_s}{a} \right)_{max} \equiv \frac{t}{\nu_1 E_R} \frac{1}{(2\pi)^{3/2} O_{00}(v_0)^2 O_{11}(v_0)}.$$

This quantity is shown for filling factor $\nu_1 = 1$ as the dashed line in Fig. 13.

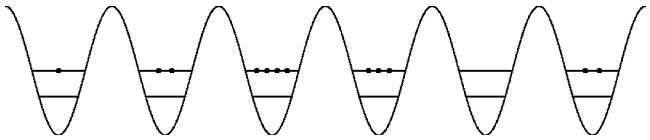

FIG. 14. Typical initial state $|i\rangle$ for the lifetime estimate in the narrowband limit. All atoms are residing in the first band, localized in the wells. In this particular case the filling factors are $\nu_0 = 0$, $\nu_1 = 1$, and $\nu_{n>1} = 0$.

B. Narrowband limit

From the discussion above it is clear that for deep enough potentials the validity of the wideband analysis breaks down unless $\nu_1(a_s/a)$ is extremely small. An alternative starting point is when $\nu_1 U \gg t$ while the filling factors for the zeroth and the second band are small, i.e., $\nu_0, \nu_2 \ll 1$. Keeping terms of order $\nu_1 U$, the relevant unperturbed Hamiltonian to start from is in this case one where tunneling events in the two lowest bands are completely ignored whereas interactions between atoms are considered only for atoms interacting with particles in the first band. Hence, one finds

$$\begin{aligned} \hat{H}_0 = & \sum_{n=0,1} \sum_m E_n(m) \hat{n}_n(m) + U_{0x} \sum_m \hat{n}_0(m) \hat{n}_1(m) \\ & + \frac{1}{2} U_{xx} \sum_m \hat{n}_1(m) [\hat{n}_1(m) - 1] \\ & + E_R \sum_{n>1} \int d\xi \, \hat{\psi}^\dagger_n(\xi) \left(-\frac{\partial^2}{\partial \xi^2} + v_{0x}(\xi) \right) \hat{\psi}_n(\xi) \\ & + 2U \sum_{n>1} \int d\xi \, \hat{\psi}^\dagger_1(\xi) \hat{\psi}_1(\xi) \hat{\psi}^\dagger_n(\xi) \hat{\psi}_n(\xi). \end{aligned} \tag{22}$$

Here the number operators $\hat{n}_n(m) \equiv \hat{a}^\dagger_n(m) \hat{a}_n(m)$ have been introduced.

The initial state is a product of Fock states with definite numbers of particles in the first band of each well as depicted in Fig. 14. Here, each well m initially has n_m atoms in the first band, i.e.,

$$|i\rangle = \prod_m \frac{[\hat{a}^\dagger_1(m)]^{n_m}}{\sqrt{n_m!}} |0\rangle.$$

The final state is one where the population has changed such that, for a particular well, denoted by r, one particle has decayed from the first band down to the zeroth while another atom, in order to conserve energy, ends up in a Bloch state of the nth $(n > 1)$ band, i.e.,

$$|f\rangle = \frac{\hat{a}^\dagger_0(r) \hat{a}^\dagger_{nk} \hat{a}_1(r)^2}{\sqrt{n_r(n_r - 1)}} |i\rangle.$$

This state is not an exact eigenstate of the unperturbed Hamiltonian in Eq. (22) but an approximate one. The correction to the Bloch wave functions for $n > 1$, which will later occur in the overlap integrals, is, however, only of the order $U/v_{0x} \ll 1$ and can thus be ignored. What is more important is the associated energy shift since this affects the positions of the band edges of the nth band. This, in turn, can have

impact on the lifetime since it affects the final density of states. Hence, one can replace the two last terms in the unperturbed Hamiltonian (22) by a term diagonal in the band index n:

$$\hat{H}_0 = \sum_{n=0,1} \sum_m E_n(m)\hat{n}_n(m) + U_{0x}\sum_m \hat{n}_0(m)\hat{n}_1(m) + \frac{1}{2}U_{xx}\sum_m \hat{n}_1(m)[\hat{n}_1(m)-1] + \sum_{n>1,k} [\epsilon_n(k) + \nu_1\Delta_{nk}]\hat{n}_{nk}. \tag{23}$$

Here, the first-order (Hartree) shift Δ_{nk} in energy due to interactions between an atom in the nth Bloch band and the atoms in the first band has been incorporated,

$$\Delta_{nk} \equiv U\int d\xi |u_{nk}(\xi) + u_{n,-k}(\xi)|^2 |\tilde{\phi}_1(\xi)|^2.$$

For first-order decay one needs only the matrix element $\langle f|\hat{V}|i\rangle$ from which the rate follows:

$$w = \frac{2\pi}{\hbar}U^2 n_r(n_r-1)\left|\int d\xi\, u^*_{nk}(\xi)\tilde{\phi}^*_0(\xi)\tilde{\phi}_1(\xi)^2\right|^2 \rho(\epsilon_n(k)). \tag{24}$$

To present a comprehensive numerical analysis of this decay rate is prohibitive due to the large number of parameters entering expression Eq. (24). Thus, for sake of illustration, we will here restrict the discussion to unit filling factor in the second band, i.e., $\nu_1=1$. Further, we use $(a_s/a)=1/100$ which is a reasonable value from an experimental point of view. The lattice depths in the transverse directions will be chosen slightly larger than in the x direction, i.e., we choose $v_{0y}=v_{0z}=v_{0x}+1$.

The results of the calculation, using wave functions obtained from band-structure calculations, are shown in Fig. 15 which plots the ratio between the hopping rate and decay rate $t_1/(\hbar w)$. The different solid lines correspond to different numbers of particles initially in the well. The cases $n_r=2,3,4,5$ are shown, $n_r=2$ having the longest lifetime and $n_r=5$ having the shortest. The dashed line shows the ratio $t_1/(\nu_1 U)$ which should be less than unity for the expression to be valid. As a comparison, the resulting lifetime obtained in the wideband limit Eq. (21) is also shown as the dash-dotted line.

The most interesting part of the result shown in Fig. 15 is the sudden decay of the lifetime. This is, as was the case in the wideband limit, a result of the diverging density of states $\rho(\epsilon_2(k))$ near the band edge. For lattice potentials deeper than $v_{0x}\approx 20$, there is no phase space (no available final energy levels for the excited particle) available for the first-order decay. To find out the lifetime for larger values of v_{0x}, second-order perturbation theory is needed.

Consider again the same initial state $|i\rangle$ as above. Adhering to energy conservation arguments, there are three different, mutually orthogonal, final states reachable through a second-order process,

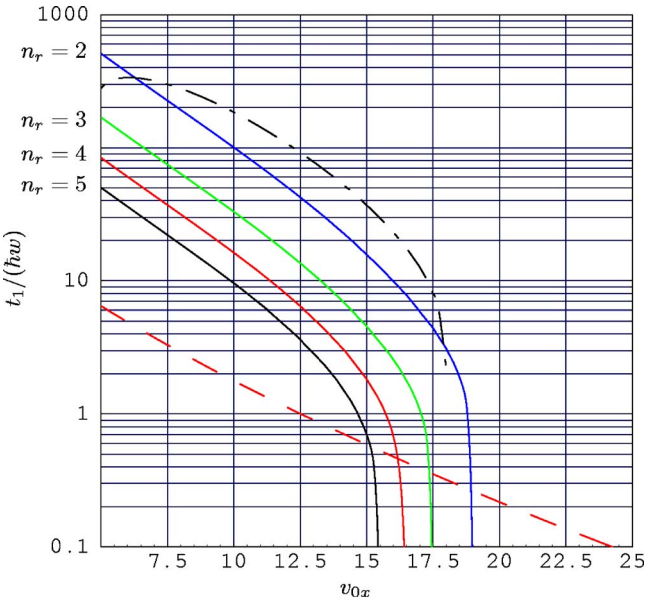

FIG. 15. (Color online) First-order lifetime w^{-1} for a 1D system with filling factor $\nu_1=1$ and $(a_s/a)=1/100$ in the narrowband limit according to Eq. (24). The solid lines show the ratio between the lifetime and the time scale for hopping $(\hbar t_1^{-1})$ for n_r particles in well r. From top to bottom, (blue) $n_r=2$; (green) $n_r=3$; (red) $n_r=4$; (black) $n_r=5$. The dashed line shows the ratio $t_1/\nu_1 U$ which should be less than unity for perturbation theory to be valid. The dot-dashed line shows the result obtained by using the wideband formula in Eq. (21) with the same parameters.

$$|f_1\rangle = \frac{\hat{a}^\dagger_{nk}\hat{a}^\dagger_0(r)^2\hat{a}_1(r)^3}{\sqrt{2n_r(n_r-1)(n_r-2)}}|i\rangle,$$

$$|f_2\rangle = \frac{\hat{a}^\dagger_{nk}\hat{a}^\dagger_0(r)^3\hat{a}_1(r)^4}{\sqrt{6n_r(n_r-1)(n_r-2)(n_r-3)}}|i\rangle,$$

$$|f_3\rangle = \frac{\hat{a}^\dagger_{n'k},\hat{a}^\dagger_{nk}\hat{a}^\dagger_0(r)^2\hat{a}_1(r)^4}{\sqrt{2n_r(n_r-1)(n_r-2)(n_r-3)}}|i\rangle.$$

The corresponding decay rates $w_{1,2,3}$ are obtained from the textbook relation

$$w_i = \frac{2\pi}{\hbar}\left|\sum_m \frac{\langle f_i|V|m\rangle\langle m|V|i\rangle}{\epsilon_i-\epsilon_m}\right|^2 \rho(\epsilon_f).$$

Numerical evaluations of the decay rates reveal that the dominant contribution to the total decay rate $w_{tot}=w_1+w_2+w_3$ comes from w_1. The reason for this is easily understood; the contribution from w_2 is small due to destructive interference of time-reversed processes while the smallness of w_3 is due to the smallness of the overlap integrals, which in turn can be understood from parity considerations.

The decay rate w_1 is shown in Fig. 16. As can be seen, it is possible to achieve lifetimes considerably larger than the inverse of the hopping energy, thus justifying the validity of the Hamiltonians in Eqs. (12) and (14).

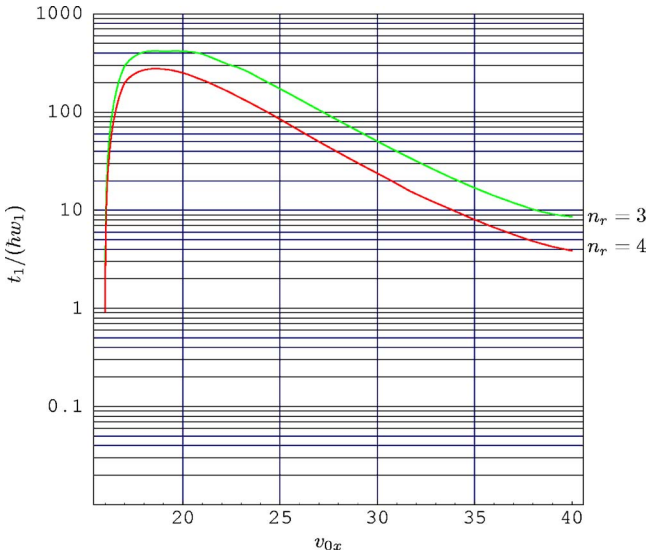

FIG. 16. (Color online) Second order lifetime w_1^{-1} for a 1D system with filling factor $\nu_1=1$ and $(a_s/a)=1/100$ in the narrow-band limit according to Eq. (24). The solid lines show the ratio between the lifetime and the time scale for hopping $(\hbar t_1^{-1})$ for n_r particles in well r. From top to bottom: top (green), $n_r=3$; bottom (red), $n_r=4$.

VII. CONCLUSIONS

By extending the usual mapping to the bosonic Hubbard model of ultracold atoms in an optical lattice to incorporate higher Bloch bands, effective Hamiltonians governing the dynamics of atoms in the first Bloch band(s) have been obtained. These Hamiltonians resemble previously studied bosonic Hubbard Hamiltonian but differ in two important respects.

(1) Atoms in the first excited band are labeled by three possible flavors X,Y,Z. The dynamics is such that X particles can (to a good approximation) move only in the x direction, etc.

(2) Flavor-changing collisions of atoms on the same site leading to conversion of the form $XX \rightarrow YY$, etc. occur.

By appropriate choices of the lattice depths in the different directions the number of flavors and the effective dimensionality (equal to the number of flavors) of the system can be changed. To obtain values of the relevant parameters, such as hopping energy and interaction energies, entering these effective Hamiltonians we have solved the time-independent Schrödinger equation (Mathieu equation).

The effective Hamiltonians in two and three dimensions also show, apart from the usual global U(1) gauge symmetry, a set of Z_2-gauge symmetries intermediate between local and global. The ground state in the 3D (three-flavor) case also displays a chiral symmetry breaking and an additional accidental ground-state degeneracy associated with different planar chiral ordering.

The phase diagrams for two particular cases relevant for experiment have been sketched using mean-field theory, indicating quantum phase transitions between Mott insulating and superfluid states.

Using time-dependent perturbation theory up to second order in the interatomic interactions the lifetime of the atoms in the excited bands has been estimated. The results show that lifetimes considerably longer (orders of magnitude) than relevant dynamical time scales can obtain. This suggests that it may be possible to realize quasiequilibrium in the subspaces of metastable states spanned by the effective Hamiltonians. Finally, we would like to stress that the mean-field theory used to draw the phase diagram is able to describe only the most simple scenario with a transition from a Mott state to a superfluid state with order parameter $\langle X\rangle \neq 0$. It is well known [14–18] that other multiflavor bosonic Hubbard models such as the two-species Bose-Hubbard model show a rich phase diagram with phases that cannot be described in this simple approximation. The present model, already rich at the mean-field level, warrants further study. In particular, we have pointed out potential connections to certain classes of models of frustrated spins [21–24] and Bose metals [25] that also have an infinite but subextensive number of Z_2-gauge symmetries and as a result exhibit dimensional reduction and exotic phases. With the microscopic Hamiltonian developed here, these connections can and should now be pursued in detail.

ACKNOWLEDGMENTS

The authors wish to acknowledge M.-C. Cha, K. Sengupta, N. Read, and S. Sachdev for many useful discussions. A.I. was in part supported by The Swedish Foundation for International Cooperation in Research and Higher Education (STINT) and SMG by the National Science Foundation through NSF Grant No. DMR-0342157.

APPENDIX

Here we provide a detailed derivation of the density distribution one expects to observe in the various phases and the different ways of measuring the density-density correlations in the released cloud of atoms.

If the system is in a many-body quantum state $|\Phi\rangle$ when the trap is released at time $t=0$ the density distribution of atoms at a later time t is given by

$$\langle n(\mathbf{r})\rangle_t = \langle\Phi|U^\dagger(t)n(\mathbf{r})U(t)|\Phi\rangle, \tag{A1}$$

where $U(t)$ is the time-evolution operator of the released system $U(t)=\exp(-i\hbar^{-1}Ht)$. To measure the quantity in Eq. (A1) one has to, in general, perform several measurements starting with the same trapped state $|\Phi\rangle$ each time. An exception to this is when the ground state is to a good approximation a macroscopically occupied single-particle state. This is typically the case for a superfluid system and a single measurement gives a good approximation of $\langle n(\mathbf{r})\rangle_t$. For a weakly interacting dilute gas of atoms the interactions between atoms can be ignored during the expansion of the cloud and the time-evolution operator in Eq. (A1) can be replaced by the free time-evolution operator $U_0(t)$. Expanding in the momentum components one finds

$$\langle n(\mathbf{r})\rangle_t = \int \frac{d\mathbf{k}_1}{(2\pi)^3}\int \frac{d\mathbf{k}_2}{(2\pi)^3} e^{-i(\mathbf{k}_1-\mathbf{k}_2)\cdot[\mathbf{r}-(\hbar t/2m)(\mathbf{k}_1+\mathbf{k}_2)]} \times \langle\Phi|\psi^\dagger_{\mathbf{k}_1}\psi_{\mathbf{k}_2}|\Phi\rangle. \quad \text{(A2)}$$

For a system of linear size L and for times $\hbar t \gg mL^2$ the stationary-phase approximation gives

$$\langle n(\mathbf{r})\rangle_t \approx \left(\frac{m}{ht}\right)^3 \langle\Phi|n_{\mathbf{Q}(\mathbf{r})}|\Phi\rangle, \quad \mathbf{Q}(\mathbf{r}) \equiv \frac{m\mathbf{r}}{\hbar t}. \quad \text{(A3)}$$

Measuring the density of atoms after a long time of flight t thus corresponds to a measurement of momentum distribution of the state $|\Phi\rangle$ prior to trap release.

In a typical experiment one takes an absorbtion image of the released cloud. This means that only the integrated column density is measured, i.e., if an image of, say, the x-y plane is taken, one measures

$$I(x,y) = \int dz \langle n(\mathbf{r})\rangle_t = \left(\frac{m}{ht}\right)^2 \int \frac{dQ_z}{2\pi}\langle\Phi|n_{\mathbf{Q}(\mathbf{r})}|\Phi\rangle.$$

In the next subsection we derive the momentum distribution $\langle\Phi|n_{\mathbf{Q}(\mathbf{r})}|\Phi\rangle$ for the superfluid states in the two- and three-flavor systems at zero temperature where Z_2 symmetry is broken.

1. 2D, two flavors, superfluid state, $T=0$

For the two-flavor case the system is comprised of 2D planes with uncorrelated ground states. A superfluid state of a single 2D plane can be described by a wave function with M particles in a single state,

$$|\Phi\rangle = (M!)^{-1/2}(a^\dagger_{SF})^M|0\rangle,$$

$$a^\dagger_{SF} \equiv \frac{1}{\sqrt{2N}}\sum_{m=1}^{N}\sum_{n=1}^{N}(\alpha_{mn}X^\dagger_{mn} + \beta_{mn}Y^\dagger_{mn}). \quad \text{(A4)}$$

The subscripts m and n denote the coordinates, rows and columns, in the lattice while α and β are phase factors $|\alpha| = |\beta| = 1$ determining the phase of the wave function on a given site.

To evaluate the momentum distribution we expand the field operators $\psi^\dagger_{\mathbf{Q}}$ and $\psi_{\mathbf{Q}}$ in terms of the localized creation and destruction operators $X^\dagger_{mn}$, Y_{mn}, etc., where the subscripts m and n, respectively, denote the row and column for the site on which the operator is acting. For a general state $|\Phi\rangle$ [not necessarily the state in Eq. (A4)] we find

$$\begin{aligned}\langle\Phi|\psi^\dagger_{\mathbf{Q}}\psi_{\mathbf{Q}}|\Phi\rangle &= \int d\mathbf{r}_1\, d\mathbf{r}_2\, e^{i\mathbf{Q}\cdot(\mathbf{r}_1-\mathbf{r}_2)}\langle\Phi|\psi^\dagger(\mathbf{r}_1)\psi(\mathbf{r}_2)|\Phi\rangle \\ &= \sum_{m_1n_1}\sum_{m_2n_2}\int d\mathbf{r}_1\int d\mathbf{r}_2\, e^{i\mathbf{Q}\cdot(\mathbf{r}_1-\mathbf{r}_2)} \\ &\quad\times\langle\Phi|[X^\dagger_{m_1n_1}\phi^x_{m_1n_1}(\mathbf{r}_1)^* + Y^\dagger_{m_1n_1}\phi^y_{m_1n_1}(\mathbf{r}_1)^*] \\ &\quad\times[X_{m_2n_2}\phi^x_{m_2n_2}(\mathbf{r}_2) + Y_{m_2n_2}\phi^y_{m_2n_2}(\mathbf{r}_2)]|\Phi\rangle. \end{aligned} \quad \text{(A5)}$$

The localized Wannier orbitals $\phi^x_{nm}(\mathbf{r})$ and $\phi^y_{nm}(\mathbf{r})$ can be rewritten

$$\phi^x_{mn}(\mathbf{r}) = (-1)^n\phi^x_0(\mathbf{r} - na\hat{x} - ma\hat{y}),$$

$$\phi^y_{mn}(\mathbf{r}) = (-1)^m\phi^y_0(\mathbf{r} - na\hat{x} - ma\hat{y})$$

with the prefactors $(-1)^{n(m)}$ coming from the gauge choice in the inital way of writing the Hamiltonian in Eq. (2). Carrying out the Fourier integrals we find

$$\begin{aligned}\langle\Phi|\psi^\dagger_{\mathbf{Q}}\psi_{\mathbf{Q}}|\Phi\rangle = \sum_{m_1n_1}\sum_{m_2n_2} e^{i\mathbf{Q}\cdot(\mathbf{R}_1-\mathbf{R}_2)}\langle\Phi|[&X^\dagger_{m_1n_1}(-1)^{n_1}\tilde{\phi}^x_0(\mathbf{Q})^* \\ &+ Y^\dagger_{m_1n_1}(-1)^{m_1}\tilde{\phi}^y_0(\mathbf{Q})^*][X_{m_2n_2}(-1)^{n_2}\tilde{\phi}^x_0(\mathbf{Q}) \\ &+ Y_{m_2n_2}(-1)^{m_2}\tilde{\phi}^y_0(\mathbf{Q})]|\Phi\rangle. \end{aligned} \quad \text{(A6)}$$

Here the position vectors $\mathbf{R}_1$ and $\mathbf{R}_2$ are shorthand for the lattice vectors

$$\mathbf{R}_1 \equiv n_1a\hat{x} + m_1a\hat{y}, \quad \mathbf{R}_2 \equiv n_2a\hat{x} + m_2a\hat{y},$$

and $\tilde{\phi}^{x(y)}_0(\mathbf{Q})$ denote the Fourier transforms of the onsite wave functions. In the harmonic oscillator approximation these are given by

$$\tilde{\phi}^x_0(\mathbf{Q}) = \pi^{3/4}\gamma^{-5/2}Q_x e^{-(Q_x^2+Q_y^2+Q_z^2)/2\gamma^2}, \quad \gamma^2 = \frac{2\pi\sqrt{mV_0}}{\hbar\lambda},$$

$$\tilde{\phi}^y_0(\mathbf{Q}) = \pi^{3/4}\gamma^{-5/2}Q_y e^{-(Q_x^2+Q_y^2+Q_z^2)/2\gamma^2}. \quad \text{(A7)}$$

To evaluate $\langle\Phi|\psi^\dagger_{\mathbf{Q}}\psi_{\mathbf{Q}}|\Phi\rangle$ we need to calculate expectation values of the kind $\langle\Phi|X^\dagger Y|\Phi\rangle$. For the superfluid state $|\Phi\rangle$ in Eq. (A4) it is easily verified that in terms of the in-plane density $\rho \equiv M/N^2$ one gets

$$\langle\Phi|X^\dagger_{m_1n_1}X_{m_2n_2}|\Phi\rangle = \frac{\rho}{2}\alpha^*_{m_1n_1}\alpha_{m_2n_2},$$

$$\langle\Phi|X^\dagger_{m_1n_1}Y_{m_2n_2}|\Phi\rangle = \frac{\rho}{2}\alpha^*_{m_1n_1}\beta_{m_2n_2},$$

etc. Hence the term in Eq. (A6) factors and one can write it conveniently as

$$\langle\Phi|\psi^\dagger_{\mathbf{Q}}\psi_{\mathbf{Q}}|\Phi\rangle = |\tilde{\Psi}_x(\mathbf{Q})|^2 + |\tilde{\Psi}_y(\mathbf{Q})|^2 + 2\,\mathrm{Re}[\tilde{\Psi}_x(\mathbf{Q})^*\tilde{\Psi}_y(\mathbf{Q})] \quad \text{(A8)}$$

where we have defined

$$\tilde{\Psi}_x(\mathbf{Q}) \equiv \tilde{\phi}^x_0(\mathbf{Q})\sqrt{\frac{\rho}{2}}\sum_{mn} e^{-i\mathbf{Q}\cdot\mathbf{R}_{mn}}(-1)^n\alpha_{mn}, \quad \text{(A9)}$$

$$\tilde{\Psi}_y(\mathbf{Q}) \equiv \tilde{\phi}^y_0(\mathbf{Q})\sqrt{\frac{\rho}{2}}\sum_{mn} e^{-i\mathbf{Q}\cdot\mathbf{R}_{mn}}(-1)^m\beta_{mn}. \quad \text{(A10)}$$

For a system at absolute zero the phase factors α and β are aligned along rows and columns, respectively, but are randomly distributed between the lines and columns. To describe this situation we introduce two sets of fields η^x_m and η^y_n

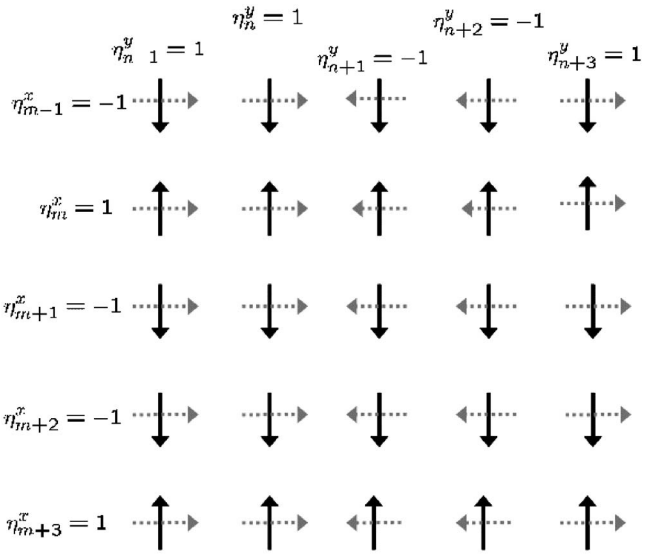

FIG. 17. Sample configuration of phases and the fields η^x_m and η^y_n for a plane in the two-flavor system at zero temperature.

which can take on values ±1. The relation between these values of the fields and the phases along rows and columns is shown in Fig. 17. Thus we can write

$$\alpha_{nm} = \eta^x_m, \quad \beta_{nm} = i\eta^y_n. \tag{A11}$$

Consider now the summations needed to evaluate $\tilde{\Psi}_x$:

$$\tilde{\Psi}_x(\mathbf{Q}) = \tilde{\phi}^x_0(\mathbf{Q})\sqrt{\frac{\rho}{2}}\sum_{mn} e^{-i\mathbf{Q}\cdot\mathbf{R}_{mn}}(-1)^n \eta^x_m \tag{A12}$$

The summation over columns (n summation) converges in the large-N limit to a sequence of δ functions,

$$\tilde{\Psi}_x \equiv 2\pi\tilde{\phi}^x_0\sqrt{\frac{N\rho}{2}}\sum_{mn}\delta(aQ_x-(2n+1)\pi)e^{-imQ_ya}\eta^x_m, \tag{A13}$$

and a similar equation can be obtained for $\tilde{\Psi}_y$. Hence

$$|\tilde{\Psi}_x|^2 = 2\pi N\frac{\rho}{2}|\tilde{\phi}^x_0|^2\sum_n \delta(aQ_x-(2n+1)\pi) \times \sum_{mm'} e^{-i(m-m')Q_ya}\eta^x_m\eta^x_{m'}.$$

Introducing $\Delta=m-m'$ the last summations can be rewritten as

$$\begin{aligned} Nf_1(Q_y,\eta^x_m) &\equiv \sum_{mm'} e^{-i(m-m')Q_ya}\eta^x_m\eta^x_{m'} \\ &= \sum_\Delta e^{-i\Delta Q_ya}\sum_m \eta^x_m\eta^x_{m-\Delta} = N \\ &\quad + \sum_{\Delta\neq 0} e^{-i\Delta Q_ya}\sum_m \eta^x_m\eta^x_{m-\Delta} \end{aligned} \tag{A14}$$

where we have defined the random momentum distribution function f_1. With the aid of Eq. (A14) we now deduce some properties of f_1. We begin with the magnitude of the function for any value of Q_y. For each nonzero value of Δ the last summation is over an uncorrelated sequence of integers ±1 and can be viewed as a 1D random walk for which we have that

$$\sum_m e^{i\pi(\eta^x_m-\eta^x_{m-\Delta})} \sim O(\sqrt{N}).$$

The summation over Δ contains $N-1$ terms which for each value of Q_y are random of magnitude $\sqrt{N}$. This is again a random walk with $N-1$ steps and we conclude that the whole expression in Eq. (A14) is of order N. This can also be seen by noting that

$$\frac{a}{2\pi}\int_{-\pi/a}^{\pi/a} dQ_y f_1(Q_y,\eta^x_m) = 1.$$

Thus for each configuration η^x_m we have a randomly oscillating function $f(Q_y,\eta^x_m)$ of unit magnitude. An example of f_1 obtained for a specific realization of η^x_m with $N=40$ is shown in Fig. 18. From Eq. (A14) it is also clear, since η^x_m and $\eta_{m-\Delta}$ are uncorrelated for nonzero Δ, that the average over allowed ground-state configurations is

$$\overline{f_1(Q_y,\eta^x_m)} \equiv \frac{1}{2^N}\sum_{\eta^x_1,\ldots,\eta^x_N=\pm 1} f_1(Q_y,\eta^x_m) = 1.$$

An important property of f_1 is that it is even in Q_y,

$$f_1(Q_y,\eta^x_m) = f_1(-Q_y,\eta^x_m).$$

This is a result of the nematic ordering between rows. $|\tilde{\Psi}_y|^2$ can be calculated in the same way as $|\tilde{\Psi}_x|^2$ and we get

$$|\tilde{\Psi}_x|^2 = \pi M|\tilde{\phi}^x_0(\mathbf{Q})|^2 f_1(Q_y,\eta^x_m)\sum_{\text{odd } n}\delta(aQ_x-n\pi),$$

$$|\tilde{\Psi}_y|^2 = \pi M|\tilde{\phi}^y_0(\mathbf{Q})|^2 f_1(Q_x,\eta^y_n)\sum_{\text{odd } m}\delta(aQ_y-m\pi).$$

The interference term, the last part of Eq. (A8), for the momentum distribution vanishes. To see this one can make use of Eqs. (A11) and (A13),

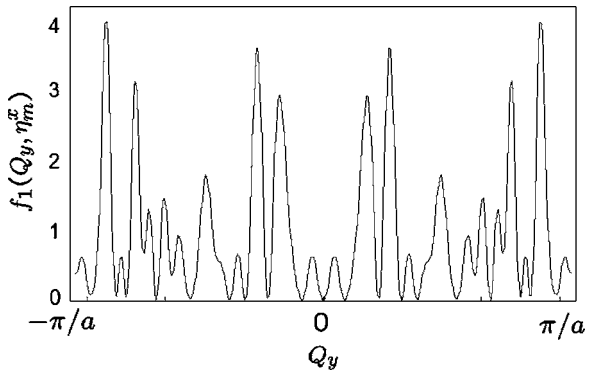

FIG. 18. Example of the random function $f_1(Q_y,\eta^x_m)$ defined in Eq. (A14).

$$2\,\mathrm{Re}[\tilde{\Psi}_x(\mathbf{Q})^*\tilde{\Psi}_y(\mathbf{Q})] = 4\pi^2\rho\tilde{\phi}_0^x\tilde{\phi}_0^y\,\mathrm{Re}\Bigg(\sum_{mn}\delta(aQ_x-(2n+1)\pi)e^{imQ_ya}\eta_m^x \times i\sum_{mn}\delta(aQ_y-(2m+1)\pi)e^{-inQ_xa}\eta_n^y\Bigg)=0.$$

2. 3D, three-flavors, superfluid state, $T=0$

For the three-flavor case at $T=0$ we consider again a state of the kind in Eq. (A4) but with

$$a_{SF}^\dagger \equiv \frac{1}{\sqrt{3}N^{3/2}}\sum_{j=1}^{N^3}(\alpha_jX_j^\dagger+\beta_jY_j^\dagger+\gamma_jZ_j^\dagger).$$

The subscript j denotes collectively the x, y, and z coordinates in the 3D lattice. As in the two-flavor case, the observed momentum distribution can be written as

$$\langle\Phi|\psi_{\mathbf{Q}}^\dagger\psi_{\mathbf{Q}}|\Phi\rangle = |\tilde{\Psi}_x(\mathbf{Q})|^2+|\tilde{\Psi}_y(\mathbf{Q})|^2+|\tilde{\Psi}_z(\mathbf{Q})|^2 + 2\,\mathrm{Re}[\tilde{\Psi}_x(\mathbf{Q})^*\tilde{\Psi}_y(\mathbf{Q})] + 2\,\mathrm{Re}[\tilde{\Psi}_y(\mathbf{Q})^*\tilde{\Psi}_z(\mathbf{Q})]+2\,\mathrm{Re}[\tilde{\Psi}_z(\mathbf{Q})^*\tilde{\Psi}_x(\mathbf{Q})] \tag{A15}$$

with

$$\tilde{\Psi}_x(\mathbf{Q})\equiv\tilde{\phi}_0^x(\mathbf{Q})\sqrt{\frac{\rho}{3}}\sum_{mno}e^{-i\mathbf{Q}\cdot\mathbf{R}_{mno}}(-1)^m\alpha_{mno},$$

$$\tilde{\Psi}_y(\mathbf{Q})\equiv\tilde{\phi}_0^y(\mathbf{Q})\sqrt{\frac{\rho}{3}}\sum_{mno}e^{-i\mathbf{Q}\cdot\mathbf{R}_{mno}}(-1)^n\beta_{mno},$$

$$\tilde{\Psi}_z(\mathbf{Q})\equiv\tilde{\phi}_0^z(\mathbf{Q})\sqrt{\frac{\rho}{3}}\sum_{mno}e^{-i\mathbf{Q}\cdot\mathbf{R}_{mno}}(-1)^o\gamma_{mno}.$$

Here the subscripts m,n,o refer to the x, y, and z coordinates in the lattice, respectively. To see how to handle the phase factors in the three-flavor case, we begin with a state without accidentally broken chiral symmetry,

$$\alpha_{mno}=\eta_{no}^x,\quad \beta_{mno}=e^{i2\pi/3}\eta_{mo}^y,\quad \gamma_{mno}=e^{i4\pi/3}\eta_{mn}^z,$$

where the random fields η_{ij} can again take on values ±1. Since the accidental chiral symmetry breaking occurs in parallel planes we can without loss of generality single out the x direction as the direction in which planes have uniform chirality (to compare with Fig. 8 make the rotation of axes $y\to z$, $z\to x$, $x\to y$ in Fig. 8). We thus introduce an additional field σ_m taking values ±1 for planes with different x coordinates m. The corresponding phase factors for such a state will be

$$\alpha_{mno}=\eta_{no}^x,\quad \beta_{mno}=e^{i\sigma_m(2\pi/3)}\eta_{mo}^y,\quad \gamma_{mno}=e^{i\sigma_m(4\pi/3)}\eta_{mn}^z. \tag{A16}$$

We can now evaluate $|\tilde{\Psi}_x|^2$ in the same way as for the two-flavor case,

$$|\tilde{\Psi}_x|^2=2\pi|\tilde{\phi}_0^x|^2\frac{M}{3}f_2(Q_y,Q_z,\eta_{no}^x)\sum_{\text{odd }m}\delta(aQ_x-m\pi). \tag{A17}$$

In Eq. (A17) $f_2(Q_y,Q_z,\eta_{no}^x)$ has been introduced,

$$f_2\equiv\frac{1}{N^2}\sum_{\substack{n_1o_1\\n_2o_2}}e^{ia(n_1-n_2)Q_y}e^{ia(o_1-o_2)Q_z}\eta_{n_1o_1}^x\eta_{n_2o_2}^x.$$

The random distribution function f_2 is the two-variable analog of the function f_1 above. An example of f_2 for a 40×40 lattice is shown in Fig. 12(a). Just as f_1, f_2 obey a sum rule,

$$\left(\frac{a}{2\pi}\right)^2\int_{-\pi/a}^{\pi/a}\int_{-\pi/a}^{\pi/a}dQ_yd\,Q_z\,f_2(Q_y,Q_z,\eta_{no}^x)=1$$

is symmetric under inversion,

$$f_2(Q_y,Q_z,\eta_{no}^x)=f_2(-Q_y,-Q_z,\eta_{no}^x),$$

and has an average equal to unity when averaged over ground states,

$$\overline{f_2(Q_y,Q_z,\eta_{no}^x)}=1.$$

The expressions for $|\tilde{\Psi}_y|^2$ and $|\tilde{\Psi}_y|^2$ are similar but the accidental ground-state degeneracy modifies the random distribution functions. Explicitly we have

$$|\tilde{\Psi}_y|^2=2\pi|\tilde{\phi}_0^y|^2\frac{M}{3}g_2^y(Q_z,Q_x,\eta_m^y,\sigma_m)\sum_{\text{odd }n}\delta(aQ_y-n\pi),$$

$$|\tilde{\Psi}_z|^2=2\pi|\tilde{\phi}_0^z|^2\frac{M}{3}g_2^z(Q_x,Q_y,\eta_m^z,\sigma_m)\sum_{\text{odd }n}\delta(aQ_z-n\pi),$$

with

$$g_2^y\equiv\sum_{\substack{m1o_1\\m_2o_2}}e^{ia[(m_1-m_2)Q_x+(o_1-o_2)Q_z]}\eta_{m_1o_1}^y\eta_{m_2o_2}^ye^{-i(2\pi/3)(\sigma_{m_1}-\sigma_{m_2})},$$

$$g_2^z\equiv\sum_{\substack{m1n_1\\m_2n_2}}e^{ia[(m_1-m_2)Q_x+(n_1-n_2)Q_y]}\eta_{m_1n_1}^z\eta_{m_2n_2}^ze^{-i(4\pi/3)(\sigma_{m_1}-\sigma_{m_2})}.$$

An example of the distribution function g_2^y is shown in Fig. 12(b). Note that due to the fields σ characterizing the different chirality of planes this distribution function is *not* symmetric under inversion. Finally we look at the interference terms in Eq. (A15):

$$\tilde{\Psi}_x^*\tilde{\Psi}_y=4\pi^2\tilde{\phi}_0^x\tilde{\phi}_0^y\frac{\rho}{3}\sum_{m,n\ \text{odd}}\times\delta(aQ_x-m\pi)\delta(aQ_y-n\pi)\sum_{n_1o_1}\sum_{m_2o_2}e^{iaQ_z(o_1-o_2)}(-1)^{n_1}\times\eta_{n_1o_1}^x(-1)^{m_2}\eta_{m_2o_2}^ye^{i(2\pi/3)\sigma_{m_2}}. \tag{A18}$$

In the above equation the summations over n_1 and m_1 constitute random walks. For the n_1 summation this is a random walk on a line with N unit steps ±1 giving rise, for each

value of o_1, to a random term of order $\sqrt{N}$. The sum over m_2 can also be viewed as a random walk for each value of o_2 but in the complex plane, each step being of unit length in any of the four directions $\pm 2\pi/3$ and $\pm 4\pi/3$. Summing over n_1 and m_2 thus yields, for each (o_1, o_2), a random term of magnitude N with a completely random phase. Thus the interference terms in Eq. (A15) (the other two terms can be treated similarly) give rise to a three-dimensional grid of lines in the released cloud where the density along any given line is randomly distributed. If the density is averaged over several shots with different ground states we have no contribution from the interference terms since $\overline{\tilde{\Psi}_x^* \tilde{\Psi}_y} = 0$.

3. Density averages and correlations, $T \gtrsim 0$

If T is large enough for thermal fluctuations to restore Z_2 symmetry but still small enough to preserve the distinction between the Mott state and the superfluid state, measuring the density distribution alone does not suffice since the δ peaks will be smeared. Instead correlations can be measured. To this end, assume we have a single physical system. At finite T this system undergoes transitions in a manifold of $\mathcal{N}$ states. Denote this manifold by the states $\{|\Phi_i\rangle\}_{i=1}^{\mathcal{N}}$. In a single shot a single one of these states will be probed. In an infinite series of experiments each of these states will be probed an infinite number of times and one can thereby measure the quantity

$$\overline{\langle \Phi | \hat{O} | \Phi \rangle} \equiv \frac{1}{\mathcal{N}} \sum_{i=1}^{\mathcal{N}} \langle \Phi_i | \hat{O} | \Phi_i \rangle. \tag{A19}$$

Here we have ignored the Boltzmann factors since the manifold we are looking at is nearly degenerate. In reality only a finite sequence of $\mathcal{M}$ experiments can be carried out and the fluctuations in $\langle \Phi | \hat{O} | \Phi \rangle$ are of concern. There are two sources of fluctuations: First, for each state $|\Phi_i\rangle$ there is quantum shot noise; and second, since not all of the $\mathcal{N}$ states will be probed there will be deviations due to not sampling the entire distribution.

If the manifold of states probed are superfluid states then $\mathcal{N} = O([2d]^{Nd})$ with d being the dimensionality of the system. Since superfluid states are to a good approximation macroscopically occupied single-particle states, fluctuations due to shot noise are reduced. The remaining fluctuations are classical and expected to scale as $\mathcal{M}^{-1/2}$, and $\langle \Phi | \hat{O} | \Phi \rangle$ should in principle be possible to measure. On the other hand, if the state measured is a Mott state the manifold $\{|\Phi_i\rangle\}_{i=1}^{\mathcal{N}}$ consists typically of only a few states in which case multiple measurements reduce the quantum shot noise since each quantum state will be probed many times. We thus conclude that by making repeated measurements and averaging the results, one can measure $\langle \Phi | \hat{O} | \Phi \rangle$.

A quantity of interest to measure in this way is the correlation function

$$G(\mathbf{r}, \mathbf{r}') \equiv \overline{\langle n(\mathbf{r}) n(\mathbf{r}') \rangle_t} - \overline{\langle n(\mathbf{r}) \rangle_t} \times \overline{\langle n(\mathbf{r}') \rangle_t}.$$

Again, if $\hbar t \gg mL^2$ this is to a good approximation the same as

$$G(\mathbf{r}, \mathbf{r}') = \left(\frac{m}{ht} \right)^6 [\overline{\langle n_{\mathbf{Q}} n_{\mathbf{Q}'} \rangle} - \overline{\langle n_{\mathbf{Q}} \rangle} \times \overline{\langle n_{\mathbf{Q}'} \rangle}].$$

The disorder averages of the momentum density distributions are easy to calculate. For instance, for the two-flavor superfluid state in Eq. (A4) we have

$$\overline{\langle \Phi | n_{\mathbf{Q}} | \Phi \rangle} = \overline{|\tilde{\Psi}_x(\mathbf{Q})|^2} + \overline{|\tilde{\Psi}_y(\mathbf{Q})|^2} + 2\,\mathrm{Re}[\overline{\tilde{\Psi}_x(\mathbf{Q})^* \tilde{\Psi}_y(\mathbf{Q})}]. \tag{A20}$$

The averages in Eq. (A20) can be calculated using the representation in Eqs. (A9) and (A10),

$$\overline{|\tilde{\Psi}_x|^2} = |\tilde{\phi}_0^x|^2 \frac{\rho}{2} \sum_{\substack{m_1 n_1 \\ m_2 n_2}} e^{i\mathbf{Q}\cdot(\mathbf{R}_1 - \mathbf{R}_2)} (-1)^{n_1 + n_2} \overline{\alpha_{m_1 n_1} \alpha_{m_2 n_2}}.$$

The average means averaging over all $\alpha_{mn} = \pm 1$ (and all $\beta_{mn} = \pm i$). It follows that

$$\overline{|\tilde{\Psi}_x(\mathbf{Q})|^2} = \frac{M}{2} |\tilde{\phi}_0^x(\mathbf{Q})|^2 \overline{|\tilde{\Psi}_x(\mathbf{Q})|^2} = \frac{M}{2} |\tilde{\phi}_0^y(\mathbf{Q})|^2$$

and $\overline{\tilde{\Psi}_x(\mathbf{Q})^* \tilde{\Psi}_y(\mathbf{Q})} = 0$. Hence, for the two-flavor case we find

$$\overline{\langle \Phi | n_{\mathbf{Q}} | \Phi \rangle} = \frac{M}{2} [|\tilde{\phi}_0^x(\mathbf{Q})|^2 + |\tilde{\phi}_0^y(\mathbf{Q})|^2], \tag{A21}$$

whereas for three flavors we have

$$\overline{\langle \Phi | n_{\mathbf{Q}} | \Phi \rangle} = \frac{M}{3} [|\tilde{\phi}_0^x(\mathbf{Q})|^2 + |\tilde{\phi}_0^y(\mathbf{Q})|^2 + |\tilde{\phi}_0^z(\mathbf{Q})|^2].$$

We now turn to the evaluation of the two-point correlator which we begin by normal ordering

$$\overline{\langle n_{\mathbf{Q}} n_{\mathbf{Q}'} \rangle} = (2\pi)^3 \overline{\langle n_{\mathbf{Q}} \rangle} \delta(\mathbf{Q} - \mathbf{Q}') + \overline{\langle \psi_{\mathbf{Q}}^\dagger \psi_{\mathbf{Q}'}^\dagger \psi_{\mathbf{Q}} \psi_{\mathbf{Q}'} \rangle}.$$

The normal-ordered expectation value $\langle \psi_{\mathbf{Q}}^\dagger \psi_{\mathbf{Q}'}^\dagger \psi_{\mathbf{Q}} \psi_{\mathbf{Q}'} \rangle$ can be written in a form analogous to Eq. (A6):

$$\begin{aligned}
&\langle \Phi | \psi_{\mathbf{Q}}^\dagger \psi_{\mathbf{Q}'}^\dagger \psi_{\mathbf{Q}} \psi_{\mathbf{Q}'} | \Phi \rangle \\
&\quad = \sum_{ijkl} e^{i\mathbf{Q}\cdot(\mathbf{R}_i - \mathbf{R}_j)} e^{i\mathbf{Q}'\cdot(\mathbf{R}_k - \mathbf{R}_l)} \\
&\qquad \times \langle \Phi | [X_i^\dagger (-1)^{n_i} \tilde{\phi}_0^x(\mathbf{Q})^* + Y_i^\dagger (-1)^{m_i} \tilde{\phi}_0^y(\mathbf{Q})^*] \\
&\qquad \times [X_k^\dagger (-1)^{n_k} \tilde{\phi}_0^x(\mathbf{Q}')^* + Y_k^\dagger (-1)^{m_k} \tilde{\phi}_0^y(\mathbf{Q}')^*] \\
&\qquad \times [X_j (-1)^{n_j} \tilde{\phi}_0^x(\mathbf{Q}) + Y_j (-1)^{m_j} \tilde{\phi}_0^y(\mathbf{Q})] [X_l (-1)^{n_l} \tilde{\phi}_0^x(\mathbf{Q}') \\
&\qquad + Y_l (-1)^{m_l} \tilde{\phi}_0^y(\mathbf{Q}')] | \Phi \rangle.
\end{aligned} \tag{A22}$$

Here the subscripts i,j,k,l are collective row and column coordinates for the site index in the 2D lattice.

For the two-flavor superfluid state in Eq. (A4) (a single plane with $N \times N$ sites having a total of M particles) it is easy to verify that the expectation values of on-site operators are given by expressions of the type

$$\langle\Phi|X_i^\dagger Y_k^\dagger Y_j X_l|\Phi\rangle = \frac{M(M-1)}{4N^4}\alpha_i^*\beta_k^*\beta_j\alpha_l \approx \frac{\rho^2}{4}\alpha_i^*\beta_k^*\beta_j\alpha_l.$$

To calculate the average over disorder we have to average over $\alpha_j = \pm 1$ and $\beta_j = \pm i$. The nonzero averages are easily seen to be

$$\overline{\langle X_i^\dagger X_k^\dagger X_j X_l\rangle} = \frac{\rho^2}{4}\overline{\alpha_i^*\alpha_k^*\alpha_j\alpha_l} \tag{A23}$$

$$= \frac{\rho^2}{4}(\delta_{ik}\delta_{jl} + \delta_{ij}\delta_{kl} + \delta_{il}\delta_{kj}), \tag{A24}$$

$$\overline{\langle X_i^\dagger X_k^\dagger Y_j Y_l\rangle} = \frac{\rho^2}{4}\overline{\alpha_i^*\alpha_k^*\beta_j\beta_l} = -\frac{\rho^2}{4}\delta_{ik}\delta_{jl}, \tag{A25}$$

$$\overline{\langle Y_i^\dagger X_k^\dagger Y_j X_l\rangle} = \frac{\rho^2}{4}\overline{\beta_i^*\alpha_k^*\beta_j\alpha_l} = \frac{\rho^2}{4}\delta_{ij}\delta_{kl}, \tag{A26}$$

$$\overline{\langle Y_i^\dagger X_k^\dagger X_j Y_l\rangle} = \frac{\rho^2}{4}\overline{\beta_i^*\alpha_k^*\alpha_j\beta_l} = \frac{\rho^2}{4}\delta_{il}\delta_{kj}, \tag{A27}$$

$$\overline{\langle X_i^\dagger Y_k^\dagger Y_j X_l\rangle} = \frac{\rho^2}{4}\overline{\alpha_i^*\beta_k^*\beta_j\alpha_l} = \frac{\rho^2}{4}\delta_{il}\delta_{kj}, \tag{A28}$$

$$\overline{\langle X_i^\dagger Y_k^\dagger X_j Y_l\rangle} = \frac{\rho^2}{4}\overline{\alpha_i^*\beta_k^*\alpha_j\beta_l} = \frac{\rho^2}{4}\delta_{kl}\delta_{ij}, \tag{A29}$$

$$\overline{\langle Y_i^\dagger Y_k^\dagger X_j X_l\rangle} = \frac{\rho^2}{4}\overline{\beta_i^*\beta_k^*\alpha_j\alpha_l} = -\frac{\rho^2}{4}\delta_{ik}\delta_{jl}, \tag{A30}$$

$$\overline{\langle Y_i^\dagger Y_k^\dagger Y_j Y_l\rangle} = \frac{\rho^2}{4}\overline{\beta_i^*\beta_k^*\beta_j\beta_l} = \frac{\rho^2}{4}(\delta_{ik}\delta_{jl} + \delta_{ij}\delta_{kl} + \delta_{il}\delta_{kj}). \tag{A31}$$

Note that Eqs. (A23), (A24), (A30), and (A31) have contributions that correspond to pairs of particles propagating, the disorder average of single-particle propagation being zero due to the random orientation of phases. Using Eqs. (A22)–(A31) we can evaluate the terms in Eq. (A22) that are nonzero. We state each term contributing to the correlator in Eq. (A22) separately using subscripts to denote the specific ordered combination of operators from which the term derives:

$$\overline{\langle\Phi|\psi_{\mathbf{Q}}^\dagger\psi_{\mathbf{Q}'}^\dagger\psi_{\mathbf{Q}}\psi_{\mathbf{Q}'}|\Phi\rangle}_{XXXX} = |\phi_0^x(\mathbf{Q})|^2|\phi_0^x(\mathbf{Q}')|^2\frac{\rho^2}{4}\sum_{ij}(1 + e^{i(\mathbf{Q}+\mathbf{Q}')\cdot(\mathbf{R}_i-\mathbf{R}_j)} + e^{i(\mathbf{Q}-\mathbf{Q}')\cdot(\mathbf{R}_i-\mathbf{R}_j)}), \tag{A32}$$

$$\overline{\langle\Phi|\psi_{\mathbf{Q}}^\dagger\psi_{\mathbf{Q}'}^\dagger\psi_{\mathbf{Q}}\psi_{\mathbf{Q}'}|\Phi\rangle}_{XXYY} = -\tilde{\phi}_0^x(\mathbf{Q})^*\tilde{\phi}_0^x(\mathbf{Q}')^*\tilde{\phi}_0^y(\mathbf{Q})\tilde{\phi}_0^y(\mathbf{Q}')\frac{\rho^2}{4}\times\sum_{ij}e^{i(\mathbf{Q}+\mathbf{Q}')\cdot(\mathbf{R}_i-\mathbf{R}_j)}, \tag{A33}$$

$$\overline{\langle\Phi|\psi_{\mathbf{Q}}^\dagger\psi_{\mathbf{Q}'}^\dagger\psi_{\mathbf{Q}}\psi_{\mathbf{Q}'}|\Phi\rangle}_{YXYX} = \tilde{\phi}_0^y(\mathbf{Q})^*\tilde{\phi}_0^x(\mathbf{Q}')^*\tilde{\phi}_0^y(\mathbf{Q})\tilde{\phi}_0^x(\mathbf{Q}')\frac{M^2}{4}, \tag{A34}$$

$$\overline{\langle\Phi|\psi_{\mathbf{Q}}^\dagger\psi_{\mathbf{Q}'}^\dagger\psi_{\mathbf{Q}}\psi_{\mathbf{Q}'}|\Phi\rangle}_{YXXY} = \tilde{\phi}_0^y(\mathbf{Q})^*\tilde{\phi}_0^x(\mathbf{Q}')^*\tilde{\phi}_0^x(\mathbf{Q})\tilde{\phi}_0^y(\mathbf{Q}')\frac{\rho^2}{4}\times\sum_{ij}e^{i(\mathbf{Q}-\mathbf{Q}')\cdot(\mathbf{R}_i-\mathbf{R}_j)}, \tag{A35}$$

$$\overline{\langle\Phi|\psi_{\mathbf{Q}}^\dagger\psi_{\mathbf{Q}'}^\dagger\psi_{\mathbf{Q}}\psi_{\mathbf{Q}'}|\Phi\rangle}_{XYYX} = \tilde{\phi}_0^x(\mathbf{Q})^*\tilde{\phi}_0^y(\mathbf{Q}')^*\tilde{\phi}_0^y(\mathbf{Q})\tilde{\phi}_0^x(\mathbf{Q}')\frac{\rho^2}{4}\times\sum_{ij}e^{i(\mathbf{Q}-\mathbf{Q}')\cdot(\mathbf{R}_i-\mathbf{R}_j)}, \tag{A36}$$

$$\overline{\langle\Phi|\psi_{\mathbf{Q}}^\dagger\psi_{\mathbf{Q}'}^\dagger\psi_{\mathbf{Q}}\psi_{\mathbf{Q}'}|\Phi\rangle}_{XYXY} = \tilde{\phi}_0^x(\mathbf{Q})^*\tilde{\phi}_0^y(\mathbf{Q}')^*\tilde{\phi}_0^x(\mathbf{Q})\tilde{\phi}_0^y(\mathbf{Q}')\frac{M^2}{4}, \tag{A37}$$

$$\overline{\langle\Phi|\psi_{\mathbf{Q}}^\dagger\psi_{\mathbf{Q}'}^\dagger\psi_{\mathbf{Q}}\psi_{\mathbf{Q}'}|\Phi\rangle}_{YYXX} = -\tilde{\phi}_0^y(\mathbf{Q})^*\tilde{\phi}_0^y(\mathbf{Q}')^*\tilde{\phi}_0^x(\mathbf{Q})\tilde{\phi}_0^x(\mathbf{Q}')\frac{\rho^2}{4}\times\sum_{ij}e^{i(\mathbf{Q}+\mathbf{Q}')\cdot(\mathbf{R}_i-\mathbf{R}_j)}, \tag{A38}$$

$$\overline{\langle\Phi|\psi_{\mathbf{Q}}^\dagger\psi_{\mathbf{Q}'}^\dagger\psi_{\mathbf{Q}}\psi_{\mathbf{Q}'}|\Phi\rangle}_{YYYY} = |\phi_0^y(\mathbf{Q})|^2|\phi_0^y(\mathbf{Q}')|^2\frac{\rho^2}{4}\times\sum_{ij}(1 + e^{i(\mathbf{Q}+\mathbf{Q}')\cdot(\mathbf{R}_i-\mathbf{R}_j)} + e^{i(\mathbf{Q}-\mathbf{Q}')\cdot(\mathbf{R}_i-\mathbf{R}_j)}). \tag{A39}$$

Collecting the results of Eqs. (A21)–(A39) we find

$$G_{SF}^{2D}(\mathbf{r},\mathbf{r}') \propto (2\pi)^3\frac{M}{2}\delta(\mathbf{Q}-\mathbf{Q}')[|\tilde{\phi}_0^x(\mathbf{Q})|^2 + |\tilde{\phi}_0^y(\mathbf{Q})|^2] + \frac{\rho^2}{4}|\tilde{\phi}_0^x(\mathbf{Q})\tilde{\phi}_0^x(\mathbf{Q}') + \tilde{\phi}_0^y(\mathbf{Q})\tilde{\phi}_0^y(\mathbf{Q}')|^2\times\sum_{ij}e^{i(\mathbf{Q}-\mathbf{Q}')\cdot(\mathbf{R}_i-\mathbf{R}_j)} + \frac{\rho^2}{4}|\tilde{\phi}_0^x(\mathbf{Q})\tilde{\phi}_0^x(\mathbf{Q}') - \tilde{\phi}_0^y(\mathbf{Q})\tilde{\phi}_0^y(\mathbf{Q}')|^2\times\sum_{ij}e^{i(\mathbf{Q}+\mathbf{Q}')\cdot(\mathbf{R}_i-\mathbf{R}_j)} \tag{A40}$$

where the factor of proportionality is $(m/ht)^6$. The Fourier sums give, in the limit of an infinite lattice, sequences of δ functions,

$$\sum_{ij} e^{i(\mathbf{Q}\pm\mathbf{Q}')\cdot(\mathbf{R}_i-\mathbf{R}_j)} \to \left(\frac{2\pi N}{a}\right)^2 \sum_i \delta([\mathbf{Q}\pm\mathbf{Q}'] - \mathbf{G}_i),$$

where $\mathbf{G}_i$ are reciprocal lattice vectors. The most interesting part of Eq. (A40) is the last term which comes from the pairlike propagation. This can be used as a signature to detect the superfluid phase even if thermal disorder has restored the Z_2 symmetry.

For comparison we also look at the 2D (two-flavor) Mott state. For simplicity we consider unit filling. There are three scenarios for the unit filling Mott state that need to be considered: (a) a ferromagnetic Mott state, i.e., all atoms of the same flavor; (b) an antiferromagnetic Mott state, X flavor and Y flavor on alternating sites; and (c) a thermally disordered Mott state with random occupation of X and Y flavors on each site.

In the ferromagnetic Mott state at unit filling $M=N^2$ we have two degenerate ground states $|\Phi_1\rangle=\Pi_i X_i^\dagger|0\rangle$ and $|\Phi_2\rangle=\Pi_i Y_i^\dagger|0\rangle$ and the average in Eq. (A19) is trivial to evaluate:

$$\overline{\langle\Phi|n_\mathbf{Q}|\Phi\rangle} = \frac{1}{2}(\langle\Phi_1|n_\mathbf{Q}|\Phi_1\rangle + \langle\Phi_2|n_\mathbf{Q}|\Phi_2\rangle) = \frac{M}{2}(|\phi_0^x(\mathbf{Q})|^2 + |\phi_0^y(\mathbf{Q})|^2). \tag{A41}$$

The momentum correlator can be calculated using Eq. (A22). For the state $|\Phi_1\rangle$ this equation reduces to

$$\langle\Phi_1|\psi_\mathbf{Q}^\dagger\psi_{\mathbf{Q}'}^\dagger\psi_\mathbf{Q}\psi_{\mathbf{Q}'}|\Phi_1\rangle = |\tilde{\phi}_0^x(\mathbf{Q})|^2|\tilde{\phi}_0^x(\mathbf{Q}')|^2\sum_{ijkl} e^{i\mathbf{Q}\cdot(\mathbf{R}_i-\mathbf{R}_j)} \times e^{i\mathbf{Q}'\cdot(\mathbf{R}_k-\mathbf{R}_l)}\langle\Phi_1|X_i^\dagger X_k^\dagger X_j X_l|\Phi_1\rangle. \tag{A42}$$

There are two pairings of operators that contribute to the average,

$$\langle\Phi_1|X_i^\dagger X_k^\dagger X_j X_l|\Phi_1\rangle = (1-\delta_{ik})(\delta_{ij}\delta_{kl} + \delta_{il}\delta_{kj}).$$

The term $(1-\delta_{ik})$ results from having only one particle at each site but we will ignore this term (and terms similar to it in what follows) since its relative contribution is of order $1/N^2$. The disorder average contains only two states, yielding

$$\overline{\langle\Phi|\psi_\mathbf{Q}^\dagger\psi_{\mathbf{Q}'}^\dagger\psi_\mathbf{Q}\psi_{\mathbf{Q}'}|\Phi\rangle} = \frac{1}{2}[|\tilde{\phi}_0^x(\mathbf{Q})|^2|\tilde{\phi}_0^x(\mathbf{Q}')|^2 + |\tilde{\phi}_0^y(\mathbf{Q})|^2|\tilde{\phi}_0^y(\mathbf{Q}')|^2] \times\sum_{ik}(1+e^{i(\mathbf{Q}-\mathbf{Q}')\cdot(\mathbf{R}_i-\mathbf{R}_k)}). \tag{A43}$$

The correlation function for the ferromagnetic Mott state is thus

$$G_{FM}^{2D}(\mathbf{r},\mathbf{r}') \propto (2\pi)^3\delta(\mathbf{Q}-\mathbf{Q}')\frac{M}{2}[|\phi_0^x(\mathbf{Q})|^2 + |\phi_0^y(\mathbf{Q})|^2] + \frac{M^2}{4}[|\phi_0^x(\mathbf{Q})|^2 - |\phi_0^y(\mathbf{Q})|^2][|\phi_0^x(\mathbf{Q}')|^2 - |\phi_0^y(\mathbf{Q}')|^2] + \frac{1}{2}[|\tilde{\phi}_0^x(\mathbf{Q})|^2|\tilde{\phi}_0^x(\mathbf{Q}')|^2 + |\tilde{\phi}_0^y(\mathbf{Q})|^2|\tilde{\phi}_0^y(\mathbf{Q}')|^2]\sum_{ik} e^{i(\mathbf{Q}-\mathbf{Q}')\cdot(\mathbf{R}_i-\mathbf{R}_k)}. \tag{A44}$$

In the antiferromagetic Mott state the disorder average is again over two states. Dividing the 2D lattice into two sublattices A and B, these states are $|\Phi_1\rangle=\Pi_{i\in A}\Pi_{j\in B}X_i^\dagger Y_j^\dagger|0\rangle$ and $|\Phi_2\rangle=\Pi_{j\in A}\Pi_{i\in B}X_i^\dagger Y_j^\dagger|0\rangle$. For the momentum density we have

$$\langle\Phi_1|n_\mathbf{Q}|\Phi_1\rangle = \langle\Phi_2|n_\mathbf{Q}|\Phi_2\rangle = \frac{M}{2}[|\tilde{\phi}_0^x(\mathbf{Q})|^2 + |\tilde{\phi}_0^y(\mathbf{Q})|^2];$$

hence we find again that

$$\overline{\langle\Phi|n_\mathbf{Q}|\Phi\rangle} = \frac{M}{2}[|\tilde{\phi}_0^x(\mathbf{Q})|^2 + |\tilde{\phi}_0^y(\mathbf{Q})|^2].$$

The normal-ordered two-point correlator can again be written in the form of Eq. (A22) and has six nonzero contributions. The disorder average over the two states will in this case make no difference since the two different states always give the same contribution and it is enough to consider one of them:

$$\langle\Phi_1|\psi_\mathbf{Q}^\dagger\psi_{\mathbf{Q}'}^\dagger\psi_\mathbf{Q}\psi_{\mathbf{Q}'}|\Phi_1\rangle_{XXXX} = |\tilde{\phi}_0^x(\mathbf{Q})|^2|\tilde{\phi}_0^x(\mathbf{Q}')|^2\left(\frac{M^2}{4} + \sum_{i\in A j\in A} e^{i(\mathbf{Q}-\mathbf{Q}')\cdot(\mathbf{R}_i-\mathbf{R}_j)}\right), \tag{A45}$$

$$\langle\Phi_1|\psi_\mathbf{Q}^\dagger\psi_{\mathbf{Q}'}^\dagger\psi_\mathbf{Q}\psi_{\mathbf{Q}'}|\Phi_1\rangle_{YYYY} = |\tilde{\phi}_0^y(\mathbf{Q})|^2|\tilde{\phi}_0^y(\mathbf{Q}')|^2\left(\frac{M^2}{4} + \sum_{i\in B j\in B} e^{i(\mathbf{Q}-\mathbf{Q}')\cdot(\mathbf{R}_i-\mathbf{R}_j)}\right), \tag{A46}$$

$$\langle\Phi_1|\psi_\mathbf{Q}^\dagger\psi_{\mathbf{Q}'}^\dagger\psi_\mathbf{Q}\psi_{\mathbf{Q}'}|\Phi_1\rangle_{XYXY} = \frac{M^2}{4}|\tilde{\phi}_0^x(\mathbf{Q})|^2|\tilde{\phi}_0^y(\mathbf{Q}')|^2, \tag{A47}$$

$$\langle\Phi_1|\psi_\mathbf{Q}^\dagger\psi_{\mathbf{Q}'}^\dagger\psi_\mathbf{Q}\psi_{\mathbf{Q}'}|\Phi_1\rangle_{XYYX} = \tilde{\phi}_0^x(\mathbf{Q})^*\tilde{\phi}_0^y(\mathbf{Q}')^*\tilde{\phi}_0^y(\mathbf{Q})\tilde{\phi}_0^x(\mathbf{Q}')\sum_{i\in A j\in B} e^{i(\mathbf{Q}-\mathbf{Q}')\cdot(\mathbf{R}_i-\mathbf{R}_j)}, \tag{A48}$$

$$\langle\Phi_1|\psi_\mathbf{Q}^\dagger\psi_{\mathbf{Q}'}^\dagger\psi_\mathbf{Q}\psi_{\mathbf{Q}'}|\Phi_1\rangle_{YXYX} = \frac{M^2}{4}|\tilde{\phi}_0^y(\mathbf{Q})|^2|\tilde{\phi}_0^x(\mathbf{Q}')|^2, \tag{A49}$$

$$\langle\Phi_1|\psi_{\mathbf{Q}}^\dagger\psi_{\mathbf{Q}'}^\dagger\psi_{\mathbf{Q}}\psi_{\mathbf{Q}'}|\Phi_1\rangle_{YXXY} = \tilde{\phi}_0^y(\mathbf{Q})^*\tilde{\phi}_0^x(\mathbf{Q}')^*\tilde{\phi}_0^x(\mathbf{Q})\tilde{\phi}_0^y(\mathbf{Q}')\sum_{i\in Aj\in B} e^{i(\mathbf{Q}-\mathbf{Q}')\cdot(\mathbf{R}_j-\mathbf{R}_i)}. \tag{A50}$$

Hence, we find for the 2D antiferromagnetic Mott state at unit filling the correlation function

$$\begin{aligned} G_{AFM}^{2D}(\mathbf{r},\mathbf{r}') \propto (2\pi)^3\delta(\mathbf{Q}-\mathbf{Q}')\frac{M}{2}[|\tilde{\phi}_0^x(\mathbf{Q})|^2+|\tilde{\phi}_0^y(\mathbf{Q})|^2] \\ + 2\,\mathrm{Re}[\tilde{\phi}_0^x(\mathbf{Q})^*\tilde{\phi}_0^y(\mathbf{Q}')^*\tilde{\phi}_0^y(\mathbf{Q})\tilde{\phi}_0^x(\mathbf{Q}')] \\ \times\sum_{i\in Aj\in B}\cos[(\mathbf{Q}-\mathbf{Q}')\cdot(\mathbf{R}_i-\mathbf{R}_j)] \\ + [|\tilde{\phi}_0^x(\mathbf{Q})|^2|\tilde{\phi}_0^x(\mathbf{Q}')|^2+|\tilde{\phi}_0^y(\mathbf{Q})|^2|\tilde{\phi}_0^y(\mathbf{Q}')|^2] \\ \times\sum_{i\in Aj\in A} e^{i(\mathbf{Q}-\mathbf{Q}')\cdot(\mathbf{R}_i-\mathbf{R}_j)}. \end{aligned} \tag{A51}$$

The Fourier sums converge in the limit of large N to

$$\begin{aligned} \sum_{i\in Aj\in B}\cos[(\mathbf{Q}-\mathbf{Q}')\cdot(\mathbf{R}_i-\mathbf{R}_j)] \\ = \frac{\pi^2N^2}{2a^2}\sum_{mn}[(-1)^n+(-1)^m]\delta\left(Q_x-\frac{n\pi}{a}\right) \\ \times\delta\left(Q_y-\frac{n\pi}{a}\right), \end{aligned}$$

$$\sum_{i\in Aj\in A} e^{i(\mathbf{Q}-\mathbf{Q}')\cdot(\mathbf{R}_i-\mathbf{R}_j)} = \frac{\pi^2N^2}{2a^2}\sum_{mn}[1+(-1)^{n+m}] \times\delta\left(Q_x-\frac{n\pi}{a}\right)\delta\left(Q_y-\frac{n\pi}{a}\right),$$

and the correlation function for the antiferromagnetic Mott state will thus have peaks at locations corresponding to half reciprocal lattice vectors.

Finally we look at the disordered Mott state where each site holds one atom but whether it is an X or a Y is random. The manifold of states to average over thus contains $\mathcal{N}=2^{N^2}$ states. Such a state can be written as

$$|\Phi\rangle = \prod_i \frac{1}{2}[X_i^\dagger(1+\eta_i)+Y_i^\dagger(1-\eta_i)]|0\rangle$$

where η_i is a random field taking on values ±1 on each site i. The disorder-averaged momentum distribution is again the same as before,

$$\begin{aligned} \overline{\langle\Phi|\psi_{\mathbf{Q}}^\dagger\psi_{\mathbf{Q}}|\Phi\rangle} = \sum_i \frac{1+\overline{\eta_i}}{2}\tilde{\phi}_0^x|(\mathbf{Q})|^2+\frac{1-\overline{\eta_i}}{2}|\tilde{\phi}_0^y(\mathbf{Q})|^2 \\ = \frac{M}{2}[\tilde{\phi}_0^x|(\mathbf{Q})|^2+|\tilde{\phi}_0^y(\mathbf{Q})|^2], \end{aligned} \tag{A52}$$

and there are six contributions to the momentum correlator:

$$\overline{\langle\Phi|\psi_{\mathbf{Q}}^\dagger\psi_{\mathbf{Q}'}^\dagger\psi_{\mathbf{Q}}\psi_{\mathbf{Q}'}|\Phi\rangle}_{XXXX} = \frac{1}{4}|\tilde{\phi}_0^x(\mathbf{Q})|^2|\tilde{\phi}_0^x(\mathbf{Q}')|^2\sum_{ik}1 + e^{i(\mathbf{Q}-\mathbf{Q}')\cdot(\mathbf{R}_i-\mathbf{R}_k)}, \tag{A53}$$

$$\overline{\langle\Phi|\psi_{\mathbf{Q}}^\dagger\psi_{\mathbf{Q}'}^\dagger\psi_{\mathbf{Q}}\psi_{\mathbf{Q}'}|\Phi\rangle}_{YYYY} = \frac{1}{4}|\tilde{\phi}_0^y(\mathbf{Q})|^2|\tilde{\phi}_0^y(\mathbf{Q}')|^2\sum_{ik}1 + e^{i(\mathbf{Q}-\mathbf{Q}')\cdot(\mathbf{R}_i-\mathbf{R}_k)}, \tag{A54}$$

$$\overline{\langle\Phi|\psi_{\mathbf{Q}}^\dagger\psi_{\mathbf{Q}'}^\dagger\psi_{\mathbf{Q}}\psi_{\mathbf{Q}'}|\Phi\rangle}_{XYXY} = \frac{M^2}{4}|\tilde{\phi}_0^x(\mathbf{Q})|^2|\tilde{\phi}_0^y(\mathbf{Q}')|^2, \tag{A55}$$

$$\overline{\langle\Phi|\psi_{\mathbf{Q}}^\dagger\psi_{\mathbf{Q}'}^\dagger\psi_{\mathbf{Q}}\psi_{\mathbf{Q}'}|\Phi\rangle}_{XYYX} = \frac{1}{4}\tilde{\phi}_0^x(\mathbf{Q})^*\tilde{\phi}_0^y(\mathbf{Q}')^*\tilde{\phi}_0^y(\mathbf{Q})\tilde{\phi}_0^x(\mathbf{Q}') \times\sum_{ik}e^{i(\mathbf{Q}-\mathbf{Q}')\cdot(\mathbf{R}_i-\mathbf{R}_k)}, \tag{A56}$$

$$\overline{\langle\Phi|\psi_{\mathbf{Q}}^\dagger\psi_{\mathbf{Q}'}^\dagger\psi_{\mathbf{Q}}\psi_{\mathbf{Q}'}|\Phi\rangle}_{YXYX} = \frac{M^2}{4}|\tilde{\phi}_0^y(\mathbf{Q})|^2|\tilde{\phi}_0^x(\mathbf{Q}')|^2, \tag{A57}$$

$$\overline{\langle\Phi|\psi_{\mathbf{Q}}^\dagger\psi_{\mathbf{Q}'}^\dagger\psi_{\mathbf{Q}}\psi_{\mathbf{Q}'}|\Phi\rangle}_{YXXY} = \frac{1}{4}\tilde{\phi}_0^y(\mathbf{Q})^*\tilde{\phi}_0^x(\mathbf{Q}')^*\tilde{\phi}_0^x(\mathbf{Q})\tilde{\phi}_0^y(\mathbf{Q}') \times\sum_{ik}e^{i(\mathbf{Q}-\mathbf{Q}')\cdot(\mathbf{R}_i-\mathbf{R}_k)}, \tag{A58}$$

resulting in a correlation function for the disordered Mott state

$$\begin{aligned} G_{DO}^{2D}(\mathbf{r},\mathbf{r}') \propto (2\pi)^3\delta(\mathbf{Q}-\mathbf{Q}')\frac{M}{2}[|\tilde{\phi}_0^x(\mathbf{Q})|^2+|\tilde{\phi}_0^y(\mathbf{Q})|^2] \\ + \frac{1}{4}|\tilde{\phi}_0^x(\mathbf{Q})^*\tilde{\phi}_0^x(\mathbf{Q}')+\tilde{\phi}_0^y(\mathbf{Q})^*\tilde{\phi}_0^y(\mathbf{Q}')|^2 \\ \times\sum_{ik}e^{i(\mathbf{Q}-\mathbf{Q}')\cdot(\mathbf{R}_i-\mathbf{R}_k)}. \end{aligned} \tag{A59}$$

4. Correlations in 3D, three flavors, $T \gtrsim 0$

We now look at the momentum correlations in the thermally disordered three-flavor superfluid phase. To evaluate the correlation function $\overline{\langle\Phi|\psi_{\mathbf{Q}}^\dagger\psi_{\mathbf{Q}'}^\dagger\psi_{\mathbf{Q}}\psi_{\mathbf{Q}'}|\Phi\rangle}$ one can write down the extension of Eq. (A22). There will be overall 81 terms in the expansion to evaluate. When taking the disorder average only 21 terms are nonzero. Note that when taking the disorder average in the three-flavor model one has to average not only over all possible π flips of the phases but also over the symmetry breaking field σ_m [see Eq. (A16)] to account for the chiral symmetry breaking as well as over the three directions in which chiral symmetry is broken. The nonzero averages one obtains in this way are shown below:

$$\overline{\langle X_i^\dagger X_k^\dagger X_j X_l\rangle} = \overline{\langle Y_i^\dagger Y_k^\dagger Y_j Y_l\rangle} = \overline{\langle Z_i^\dagger Z_k^\dagger Z_j Z_l\rangle} = \frac{\rho^2}{9}\left(\frac{1}{2}\delta_{ik}\delta_{jl} + \delta_{ij}\delta_{kl} + \delta_{il}\delta_{kj}\right), \tag{A60}$$

$$\overline{\langle X_i^\dagger X_k^\dagger Y_j Y_l\rangle} = \overline{\langle X_i^\dagger X_k^\dagger Z_j Z_l\rangle} = -\frac{1}{4}\frac{\rho^2}{9}\delta_{ik}\delta_{jl}, \tag{A61}$$

$$\overline{\langle Y_i^\dagger Y_k^\dagger X_j X_l\rangle} = \overline{\langle Y_i^\dagger Y_k^\dagger Z_j Z_l\rangle} = -\frac{1}{4}\frac{\rho^2}{9}\delta_{ik}\delta_{jl}, \tag{A62}$$

$$\overline{\langle Z_i^\dagger Z_k^\dagger Y_j Y_l\rangle} = \overline{\langle Z_i^\dagger Z_k^\dagger X_j X_l\rangle} = -\frac{1}{4}\frac{\rho^2}{9}\delta_{ik}\delta_{jl}, \tag{A63}$$

$$\overline{\langle X_i^\dagger Y_k^\dagger X_j Y_l\rangle} = \overline{\langle X_i^\dagger Z_k^\dagger X_j Z_l\rangle} = \frac{\rho^2}{9}\delta_{ij}\delta_{kl}, \tag{A64}$$

$$\overline{\langle Y_i^\dagger X_k^\dagger Y_j X_l\rangle} = \overline{\langle Y_i^\dagger Z_k^\dagger Y_j Z_l\rangle} = \frac{\rho^2}{9}\delta_{ij}\delta_{kl}, \tag{A65}$$

$$\overline{\langle Z_i^\dagger X_k^\dagger Z_j X_l\rangle} = \overline{\langle Z_i^\dagger Y_k^\dagger Z_j Y_l\rangle} = \frac{\rho^2}{9}\delta_{ij}\delta_{kl}, \tag{A66}$$

$$\overline{\langle X_i^\dagger Y_k^\dagger Y_j X_l\rangle} = \overline{\langle X_i^\dagger Z_k^\dagger Z_j X_l\rangle} = \frac{\rho^2}{9}\delta_{il}\delta_{kj}, \tag{A67}$$

$$\overline{\langle Y_i^\dagger X_k^\dagger X_j Y_l\rangle} = \overline{\langle Y_i^\dagger Z_k^\dagger Z_j Y_l\rangle} = \frac{\rho^2}{9}\delta_{il}\delta_{kj}, \tag{A68}$$

$$\overline{\langle Z_i^\dagger X_k^\dagger X_j Z_l\rangle} = \overline{\langle Z_i^\dagger Y_k^\dagger Y_j Z_l\rangle} = \frac{\rho^2}{9}\delta_{il}\delta_{kj}, \tag{A69}$$

and the desired correlator is obtained:

$$G_{SF}^{3D}(\mathbf{r},\mathbf{r}') \propto (2\pi)^3\delta(\mathbf{Q}-\mathbf{Q}')\frac{M}{3}[|\tilde{\phi}_0^x(\mathbf{Q})|^2 + |\tilde{\phi}_0^y(\mathbf{Q})|^2 + |\tilde{\phi}_0^z(\mathbf{Q})|^2] + \frac{1}{2}\frac{\rho^2}{9}[|\tilde{\phi}_0^x(\mathbf{Q})\tilde{\phi}_0^x(\mathbf{Q}') - \tilde{\phi}_0^y(\mathbf{Q})\tilde{\phi}_0^y(\mathbf{Q}')|^2 + |\tilde{\phi}_0^y(\mathbf{Q})\tilde{\phi}_0^y(\mathbf{Q}') - \tilde{\phi}_0^z(\mathbf{Q})\tilde{\phi}_0^z(\mathbf{Q}')|^2 + |\tilde{\phi}_0^z(\mathbf{Q})\tilde{\phi}_0^z(\mathbf{Q}') - \tilde{\phi}_0^x(\mathbf{Q})\tilde{\phi}_0^x(\mathbf{Q}')|^2]\sum_{ik} e^{i(\mathbf{Q}+\mathbf{Q}')\cdot(\mathbf{R}_i-\mathbf{R}_k)} + \frac{\rho^2}{9}|\tilde{\phi}_0^x(\mathbf{Q})\tilde{\phi}_0^x(\mathbf{Q}')^* + \tilde{\phi}_0^y(\mathbf{Q})\tilde{\phi}_0^y(\mathbf{Q}')^* + \tilde{\phi}_0^z(\mathbf{Q})\tilde{\phi}_0^z(\mathbf{Q}')^*|^2\sum_{ik} e^{i(\mathbf{Q}-\mathbf{Q}')\cdot(\mathbf{R}_i-\mathbf{R}_k)}. \tag{A70}$$

[1] S. Burger, F. S. Cataliotti, C. Fort, F. Minardi, M. Inguscio, M. L. Chiofalo, and M. P Tosi, Phys. Rev. Lett. **86**, 4447 (2001).
[2] F. S. Cataliotti, S. Burger, C. Fort, P. Maddaloni, F. Minardi, A. Trombettoni, A. Smerzi, and M. Inguscio, Science **293**, 843 (2001).
[3] D. Jaksch, C. Bruder, J. I. Cirac, C. W. Gardiner, and P. Zoller, Phys. Rev. Lett. **81**, 3108 (1998).
[4] C. Orzel, A. K. Tuchman, M. L. Fenselau, M. Yasuda, and M. A. Kasevich, Science **291**, 2386 (2001).
[5] M. Greiner, O. Mandel, T. Esslinger, T. W. Hansch, and I. Bloch, Nature (London) **415**, 39 (2002).
[6] M. Greiner, O. Mandel, T. W. Hansch, and I. Bloch, Nature (London) **419**, 51 (2002).
[7] J. H. Denschlag, J. E. Simsarian, H. Haffner, C. McKenzie, A. Browaeys, D. Cho, K. Helmerson, S. L. Rolston, and W. D. Phillips, J. Phys. B **35**, 3095 (2002).
[8] M. P. A. Fisher, P. B. Weichman, G. Grinstein, and D. S. Fisher, Phys. Rev. B **40**, 546 (1989).
[9] S. Sachdev, *Quantum Phase Transitions* (Cambridge University Press, Cambridge, U.K., 1999).
[10] D. van Oosten, P. van der Straten, and H. T. C. Stoof, Phys. Rev. A **63**, 053601 (2001).
[11] D. van Oosten, P. van der Straten, and H. T. C. Stoof, Phys. Rev. A **67**, 033606 (2003).
[12] S. Sachdev, K. Sengupta, and S. M. Girvin, Phys. Rev. B **66**, 075128 (2002).
[13] A. Polkovnikov, S. Sachdev, and S. M. Girvin, Phys. Rev. A **66**, 053607 (2002).
[14] G. H. Chen and Y. S. Wu, Phys. Rev. A **67**, 013606 (2003).
[15] A. B. Kuklov and B. V. Svistunov, Phys. Rev. Lett. **90**, 100401 (2003).
[16] A. Kuklov, N. Prokof'ev, and B. Svistunov, Phys. Rev. Lett. **92**, 050402 (2004).
[17] E. Altman, W. Hofstetter, E. Demler, and M. D. Lukin, New J. Phys. **5**, 113 (2003).
[18] L. M. Duan, E. Demler, and M. D. Lukin, Phys. Rev. Lett. **91**, 090402 (2003).
[19] A. Isacsson, M. C. Cha, K. Sengupta, and S. M. Girvin, Phys. Rev. B (to be published).
[20] V. W. Scarola and S. Das Sarma, Phys. Rev. Lett. **95**, 033003 (2005).
[21] Cenke Xu and J. E. Moore, Phys. Rev. Lett. **93**, 047003 (2004).
[22] Cenke Xu and J. E. Moore, Nucl. Phys. B **716**, 487 (2005).
[23] Z. Nussinov and E. Fradkin, Phys. Rev. B **71**, 195120 (2005).
[24] C. D. Batista and Z. Nussinov, e-print cond-mat/0410599.
[25] A. Paramekanti, L. Balents, and M. P. A. Fisher, Phys. Rev. B **66**, 054526 (2002).

[26] M. W. J. Romans, R. A. Duine, S. Sachdev, and H. T. C. Stoof, Phys. Rev. Lett. **93**, 020405 (2004).
[27] L. Radzihovsky, J. Park, and P. B. Weichman, Phys. Rev. Lett. **92**, 160402 (2004).
[28] S. E. Korshunov, A. Vallat, and H. Beck, Phys. Rev. B **51**, 3071 (1995).
[29] A. J. Leggett, Rev. Mod. Phys. **73**, 307 (2001).
[30] V. A. Kashurnikov, N. V. Prokofe'v, and B. V. Svistunov, Phys. Rev. A **66**, 031601(R) (2002).
[31] G. G. Batrouni, V. Rousseau, R. T. Scalettar, M. Rigol, A. Muramatsu, P. J. H. Denteneer, and M. Troyer, Phys. Rev. Lett. **89**, 117203 (2002).
[32] G. Pupillo, E. Tiesinga, and C. J. Williams, Phys. Rev. A **68**, 063604 (2003).
[33] C. Kollath, U. Schollwöck, J. von Delft, and W. Zwerger, Phys. Rev. A **69**, 031601(R) (2004).
[34] L. Pollet, S. Rombouts, K. Heyde, and J. Dukelsky, Phys. Rev. A **69**, 043601 (2004).
[35] S. M. Giampaolo, F. Illuminati, G. Mazzarella, and S. De Siena, Phys. Rev. A **70**, 061601(R) (2004).
[36] S. Wessel, F. Alet, M. Troyer, and G. G. Batrouni, Phys. Rev. A **70**, 053615 (2004).
[37] S. Bergkvist, P. Henelius, and A. Rosengren, Phys. Rev. A **70**, 053601 (2004).
[38] A. Browaeys, H. Haeffner, C. McKenzie, S. L. Rolston, K. Helmerson, and W. D. Phillips, e-print cond-mat/0504606.
[39] W. Zwerger, J. Opt. B: Quantum Semiclassical Opt. **5**, S9 (2003).
[40] K. Ziegler, Phys. Rev. A **68**, 053602 (2003).
[41] K. Sheshadri, H. R. Krishnamurthy, R. Pandit, and T. V. Ramakrishnan, Europhys. Lett. **22**, 257 (1993).
[42] J. R. Schrieffer and P. A. Wolff, Phys. Rev. **149**, 491 (1966).
[43] H. P. Büchler, M. Hermele, S. D. Huber, M. P. A. Fisher, and P. Zoller, Phys. Rev. Lett. **95**, 040402 (2005).
[44] D. Jaksch and P. Zoller, Ann. Phys. (N.Y.) **315**, 52 (2005).
[45] E. Altman, E. Demler, and M. D. Lukin, Phys. Rev. A **70**, 013603 (2004).
[46] M. Greiner, C. A. Regal, J. T. Stewart, and D. S. Jin, Phys. Rev. Lett. **94**, 110401 (2005).
[47] S. Fölling, F. Gerbier, A. Widera, O. Mandel, T. Gericke, and I. Bloch, Nature (London) **434**, 481 (2005).